RHODES UNIVERSITY

MeerKAT Observations of Three High-redshift Galaxy Clusters

by

Sinah Mokatako Manaka

Submitted in fulfilment of the
academic requirements for the degree of
Masters
in
Physics
Rhodes University, Makhanda

Supervised by Prof. O. M. Smirnov & Prof. G. Bernardi

March 2, 2023

To my family and friends

Declaration of Non-Plagiarism

I, **Sinah Mokatako Manaka** declare that

1. The research reported in this thesis, except where otherwise indicated, is my original research.

2. This thesis has not been submitted for any degree or examination at any other university.

3. This thesis does not contain other persons' data, pictures, graphs or other information, unless specifically acknowledged as being sourced from other persons.

4. This thesis does not contain other persons' writing, unless specifically acknowledged as being sourced from other researchers.

Abstract

Galaxy clusters are the largest, gravitationally-bound structures in the Universe, formed through the hierarchical merger of smaller structures. The most accepted view is that the merging process injects energy into the intracluster medium (ICM) and re-accelerates pre-existing particles and compresses magnetic fields, generating, eventually, synchrotron emission. Such radio emission appears as radio halos, i.e. central Mpc-size diffuse structures, mostly visible in merging or unrelaxed clusters and with a spatial correspondence with the thermal gas component of the ICM.

Observations have probed radio halo properties mostly for clusters with $M_{500} > 6 \times 10^{14}$ $\mathrm{M}_{\odot}$ at intermediate redshifts ($0.3 < z < 0.4$), providing support to their connection between mergers, which provide the necessary energy to re-accelerate particles via turbulence. Probing the redshift evolution of radio halos is an important test of the turbulent re-acceleration scenario, as fewer halos are expected at high redshift, given the same mass interval.

In this thesis, we present MeerKAT observations at 1.28 GHz of three high-redshift (PSZ2G254.08-58.45, PSZ2G255.60-46.18 and PSZ2G277.76-51.74, in the $0.42 \lesssim z \lesssim 0.46$ range) clusters, with masses $M_{500} \gtrsim 6.2 \times 10^{14}$ $\mathrm{M}_{\odot}$, selected for their disturbed dynamical state – inferred from existing X-ray observations. Our observations reached rms noise values between 20 and 23.5 μJy beam^{-1}, with $\sim 4''$ angular resolution. No evidence of diffuse emission is found at

full resolution. Low-resolution ($\sim 30''$) images achieved rms noise levels of 30-50 μJy beam^{-1}, amongst the deepest observations of high-redshift targets. One radio halo was detected in the least massive cluster PSZ2G254.08-58.45 extending over $\sim$ 500 kpc, with a 1.20 ± 0.08 mJy integrated flux density. We placed a $\sim$1 mJy upper limit at 95% confidence level on the radio halo flux density for the other two targets. The radio-halo detection is consistent with the recent $P_{1.4\,\mathrm{GHz}} - M_{500}$ correlation from Cuciti et al. (2021b), while the upper limit on PSZ2G255.60-46.18 is consistent with being on the correlation. On the other hand, the upper limit on PSZ2G277.76-51.74 places the radio halo well below the correlation.

Recently a 1.5 GHz survey (Giovannini et al., 2020) detected a slightly higher fraction of radio halos in clusters in the same redshift range, with power and size typically higher than what we found in our observations. Both observations are, however, not inconsistent with each other.

Our results, although with limited statistics, do not disfavour the current scenario of radio-halo formation based on the turbulent re-acceleration model.

Acknowledgments

I want to thank the people who supported and helped me throughout my Master's degree.

I am eternally grateful for the guidance, inspiration, mentorship and encouragement from my supervisors, Prof. Oleg Smirnov and Prof. Gianni Bernardi. Many thanks to Mr Benjamin Hugo, Dr Kenda Knowles and Dr Nadeem Oozeer for their participation and engagement in my research.

The financial assistance of the South African Radio Astronomy Observatory (SARAO) towards this research is hereby acknowledged (www.sarao.ac.za). I thank the staff of the Rhodes University Physics and Electronics department. I thank my colleagues and members of the RATT team for all their support, discussions, and reviews, which enabled the completion of this research.

Finally, I thank my family and friends for all their support and encouragement.

Contents

CHAPTER 1

INTRODUCTION

1.1 Galaxy Clusters

In the concordance model, Λ cold dark matter (ΛCDM), our Universe is made up of $\sim$69% dark energy, $\sim$26% dark matter and $\sim$5% of baryonic matter (Planck Collaboration et al., 2020). The model further suggests that small dark matter halos (DMHs) undergo hierarchical accretion and merging to form massive structures (Mo et al., 2010; Molnar, 2016; Planelles et al., 2016). These structures include environments known as galaxy clusters. Galaxy clusters are gravitationally-bound systems with thousands of galaxies. They have sizes of R_{500}[1] $\sim$1$-$3 Mpc and masses in the range of M_{500}[2]$\sim 10^{14} - 10^{15}$ $M_\odot$ (Diaferio et al., 2008; Kravtsov & Borgani, 2012). M_{500} represents the virialised portion of the cluster and is often used to define the total cluster mass (Arnaud et al., 2010).

Charles Messier first saw the clustering of nebulae. He observed an irregular distribution

[1] R_{500} is the radius corresponding to where the cluster's matter density is 500 times the critical density, ρ_{cr}, of the Universe at that cluster's redshift. Here, $\rho_{cr} = 3H(z)^2/(8\pi G)$.

[2] Cluster mass within R_{500}.

of the nebulae – which happened to be galaxies – in the Virgo constellation. In 1784, William Herschel found the Coma cluster through its numerous "nebulae". Later, Abell (1958) compiled the first catalogue of galaxy clusters. Although the phenomenon of galaxy clustering was known before the Abell catalogue, the data paved the way to a better understanding of extragalactic astronomy. The well-defined catalogue led to discoveries such as understanding, among others, galaxy clusters and large structure formation (Bahcall, 1999a).

Galaxy clusters form through mergers of sub-clusters that are among the most energetic events in the Universe ($\sim 10^{63}$ ergs; Ricker & Sarazin, 2001; Molnar, 2016). The merging sub-structures result from small density fluctuations that lead to the collapse of matter, accumulating and growing hierarchically over cosmic time to form massive structures. The growth of the fluctuations is described in two regimes: linear and non-linear. To introduce them, we use the initial primordial overdensity in the ΛCDM model, given as (Kravtsov & Borgani, 2012):

$$\delta(\mathbf{x}) = \frac{\rho(\mathbf{x}) - \overline{\rho}_m}{\overline{\rho}_m}, \tag{1.1}$$

where $\overline{\rho}_m$ is the mean mass density of the Universe. In the linear regime, $\delta(\mathbf{x}) << 1$, and the density perturbations are initially small and grow linearly (Peebles, 1980). In the non-linear regime, $\delta(\mathbf{x}) >> 1$ and numerical simulations are necessary to study the evolution of structures. The GAlaxies with Dark matter and Gas intEracT (GADGET; Springel, 2005) is an example of software that has produced one of the largest runs of numerical simulations for structure formation, known as the Millennium simulation (Springel et al., 2005).

Dark matter makes up ∼80% of the galaxy cluster mass with ∼20% contributed by baryons. The baryonic mass in clusters is composed of stars in galaxies and the hot intracluster medium (ICM; Lin et al., 2003) that emits in the X-ray. It is useful to divide galaxy clusters into two broad classes: relaxed and non-relaxed. Relaxed clusters have an undisturbed dynamical state while non-relaxed are in a merging and disturbed state (Molnar, 2016). In addition, disturbed galaxy clusters generally have dynamically perturbed X-ray morphology (Kapferer et al., 2006). Hence, X-ray observations can be used to study the morphology of clusters (Parekh et al., 2015; Martinez Aviles et al., 2018).

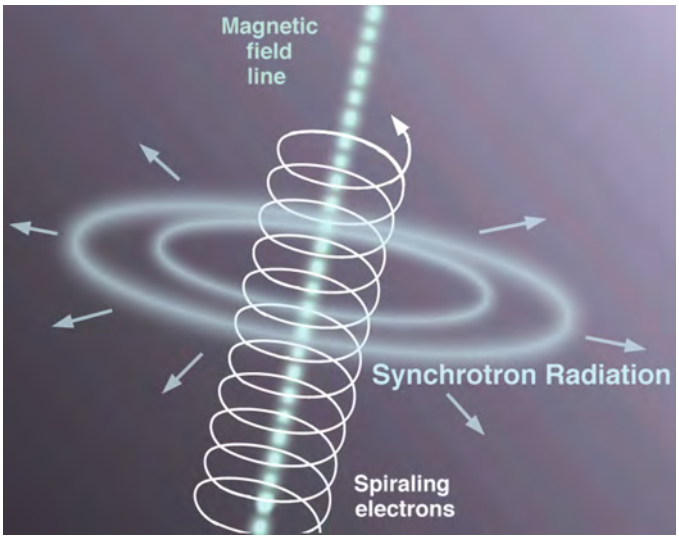

Figure 1.1: Schematic representation of synchrotron radiation. Credit: Gemini Observatory.

1.1.1 The Intracluster Medium

The ICM forms part of the baryonic mass in the form of a hot ($10^7 - 10^8$ K) and rarefied ($n_e \sim 10^{-3}$ cm^{-3}) gas that fills the cluster volume (Sarazin, 1988; Bahcall, 1999b). At this temperature range and density, the primary emission process is the thermal bremsstrahlung (free-free) emission. This emission, also called "braking radiation", is the electromagnetic radiation produced by the deceleration of electrons in electric fields of ions and nuclei. The emissivity, i.e. the energy radiated per unit volume, of the plasma at frequency ν and temperature T is given by:

$$\epsilon_\nu^{ff} = 6.8 \times 10^{-38} Z^2 n_i n_e \overline{g}_{ff} T^{-1/2} e^{-h\nu/kT} \text{ erg s}^{-1} \text{ cm}^{-3} \text{ Hz}^{-1}, \tag{1.2}$$

where Z is the ion charge, k is the Boltzmann constant, h is the Planck constant, while n_e and n_i are the number densities of electrons and ions, respectively. The parameter $\overline{g}_{ff}$ is the Gaunt factor, which is a function of (ν, T, Z) and is essential in correcting for effects in distant collisions and quantum mechanics (Sarazin, 1988). In the ICM case, Eq. 1.2 can be written as:

$$\epsilon_\nu^{ff} \propto n_e T^{1/2} e^{-h\nu/kT}, \tag{1.3}$$

which indicates that the emissivity depends on the electron number density.

Radio observations reveal the non-thermal component of the ICM in the form of relativistic electrons ($\gamma > 10^3$) and $0.1 - 10$ μG magnetic fields (Feretti et al., 2012; Brunetti & Jones, 2014;

van Weeren et al., 2019). Relativistic electrons spiralling in a magnetic field emit synchrotron radiation (see Fig. 1.1). The averaged radiated power depends on the particle energy E and magnetic field strength B (Feretti et al., 2012; Condon & Ransom, 2016):

$$\langle P \rangle \propto E^2 B^2, \tag{1.4}$$

where $\langle\rangle$ represents the average over all pitch angles, which are angles between the electron velocity and magnetic field. Eq. 1.4 indicates that the higher the magnetic field strength, the lower the energy required to generate radiation at a single frequency. The population of relativistic electrons is generally assumed to have an energy distribution that follows a power law (van Weeren et al., 2019):

$$n(E)\,\mathrm{d}E \propto E^{-p}\,\mathrm{d}E, \tag{1.5}$$

where the left-hand side is the number of electrons in a volume with energies from E to $E + \mathrm{d}E$, and p is the energy distribution which is related to the spectral index α[3] through:

$$p = 1 - 2\alpha. \tag{1.6}$$

Particle life time depends upon how quickly these electrons radiate their energy away - assuming they are not re-accelerated and, therefore, not re-energized in any way. Energy is radiated away either due to synchrotron emission or Inverse Compton (IC), i.e. relativistic electrons scattering off of Cosmic Microwave Background (CMB) photons. The typical life time due to synchrotron losses is $t_{\mathrm{age}} \lesssim 10^8$ yrs (Jaffe, 1977; Bagchi et al., 2002; Brunetti & Jones, 2014). IC losses tend to dominate at high redshift where the CMB energy density is higher:

$$\frac{dE}{dt} \propto (1+z)^4, \tag{1.7}$$

where z is the redshift. Blasi et al. (2007) illustrate that relativistic electrons have short lives and radiate energy in the region they are produced.

Although not dynamically important, cluster magnetic fields play an important role in particle acceleration and structure formation processes (Planelles et al., 2016; Donnert et al., 2018). They

[3]In this thesis, we adopt the convention α such that $S_\nu \propto \nu^\alpha$, where S_ν is the flux density at the frequency ν.

prevent transport processes such as heat conduction, mixing of gas and spread of cosmic rays. However, their origin is still debated, but a common hypothesis introduces what Rees (1987) proposed as field seeds. Initial field seeds are amplified through shocks, compression and turbulence during mergers and structure formation (Kahniashvili et al., 2013; Donnert et al., 2018). Field seeds likely originated at early times, either before recombination or in the first stars and galaxies (Rees, 2006).

A powerful way to measure cosmic magnetic fields is via Faraday rotation, the rotation of the polarization angle of the electromagnetic radiation that goes through an ionized plasma. The magnitude of the rotation is defined as the rotation measure RM (Feretti et al., 2012):

$$RM = 812 \int_{\text{source}}^{\text{observer}} n_e \, \mathbf{B} \cdot \mathrm{dl}, \tag{1.8}$$

where n_e is the electron density, B the magnetic field and dl the infinitesimal path length. RM observations have revealed that magnetic fields in clusters have intensities of the order of a few μG (Domínguez-Fernández et al., 2019; Xu & Han, 2022), with little evidence of redshift evolution, suggesting that magnetic fields may be amplified early in cosmic history (Bonafede et al., 2010; Di Gennaro et al., 2021a).

1.1.2 Detection of Galaxy Clusters

Clusters are observable at different wavelengths across the electromagnetic spectrum and this property has, historically, led to different methods to detect galaxy clusters.

1.1.2.1 X-ray Observations

Due to their massive structures, galaxy clusters attract large amounts of material in space. As this material falls towards the cluster centre, its speed increases and particles collide (Sarazin, 1988). This leads to photon emission, where the ICM shines brightly and the thermal bremsstrahlung is observed.

The hot ICM makes it simple to identify galaxy clusters at X-ray wavelengths which show the thermal origin of the gas. X-ray observations have revealed galaxy clusters as X-ray luminous

and spatially extended sources (see the first image in Fig. 1.2). They emit radiation with X-ray luminosities $L_X \sim 10^{43-45}$ erg s^{-1} in the 2−10 keV band (Sarazin, 1988).

X-ray observations provide the means to probe the dynamical state (relaxed or non-relaxed) of a cluster by analysing its X-ray morphology. Merging clusters constrain the nature of dark matter due to its gravitational attraction that leads to a series of collisions which eventually give rise to mergers (Chadayammuri et al., 2021). Hence, they probe the history of structure formation.

Historical catalogues were limited to low redshifts ($z \lesssim 0.2$; Forman et al., 1978). They revealed that galaxy clusters are the most common extragalactic X-ray sources with extended emission of Mpc-scales that does not vary in time. This implies that the emission does not result from point sources in the cluster.

The advent of new generation X-ray satellites, such as the X-ray Multi-mirror Mission-Newton (XMM-Newton; Jansen et al., 2001; Ness et al., 2014), is providing depth in understanding the physics of the ICM through observing in distant epochs. The large collecting area of XMM-Newton ($\sim$2000 cm^2 at 1 keV) will enable the discovery of clusters at redshifts up to $z \sim 2$ (Pierre et al., 2016). This illustrates the use of the X-ray band for probing the thermal history of clusters. We use the XMM-Newton observations in this thesis (see Sec. 3.1).

1.1.2.2 Optical Observations

The first catalogue of galaxy clusters was done with optical observations (Abell, 1958). Most of the radiation at this wavelength is mainly from starlight in galaxies. In this band, galaxy clusters are identified by the richness (the total number of galaxies), optical luminosity and colour, which are observables in the cluster (Allen et al., 2011; Rykoff et al., 2014, see middle panel of Fig. 1.2).

A colour-magnitude relation is constructed from the optical observables of early-type, red galaxies that dominate the cluster cores (Gladders & Yee, 2000). It demonstrates a tight linear relation which is homogeneous from cluster to cluster (Bower et al., 1992; López-Cruz et al., 2004). Thus, it is a commonly used method for cluster detection in the visible band. Interestingly, the relation is defined by its slope and intercept, which depend on the redshift (Gladders et al.,

1998). The method is, therefore, implemented by generating models of the relation at various redshifts (López-Cruz et al., 2004; Zohren et al., 2019). In other words, when the clustering of galaxies is observed in optical, the observable properties of the red galaxies can be compared with a model at a specific redshift. When the galaxies follow this model, then a cluster candidate is discovered at the so-called photometric redshift.

The advantage of this method is that it is simple to distinguish the cluster members as they appear redder than the foreground structures at a given redshift. On the other hand, background structures are more significant at redder colours. The method has yielded large cluster optical catalogues in several surveys, such as the Sloan Digital Sky Survey (Rykoff et al., 2014) and has estimated cluster photometric redshifts above 0.8 (Zohren et al., 2019).

1.1.2.3 Sunyaev-Zel'dovich Effect Observations

CMB photons that travel through a galaxy cluster can be scattered by the hot electrons in the ICM. This spectral distortion is known as the Sunyaev-Zel'dovich (SZ; Sunyaev & Zel'dovich, 1972) effect and clusters would appear as shadows against the CMB at certain radio wavelengths. Its magnitude is obtained through the so-called Compton y parameter, the line of sight integral of the electron thermal pressure energy:

$$y = \int \sigma_T \frac{n_e k T_e}{m_e c_2} \mathrm{d}l \propto P_e \mathrm{d}l, \tag{1.9}$$

where σ_T is the Thomson cross section, n_e the electron number density, the integral is along the line of sight, and T_e, m_e, P_e is the electron temperature, mass and pressure, respectively. We show an example of the SZ-signal viewed in mm wavelengths in the last panel of Fig. 1.2.

Telescopes such as the Planck satellite have produced the largest SZ-selected sample of galaxy clusters to date (Planck Collaboration et al., 2016). It has a total of 1653 detections with > 1000 confirmed clusters. The catalogue confirmed the detection of clusters at $z > 0.6$. The SZ-effect has been able to detect clusters with redshifts $z > 1$ (e.g., Kim et al., 2019). These research works indicate that the SZ-effect is sensitive and efficient for finding distant clusters.

1.1.2.4 Gravitational Lensing Observations

Large mass concentrations of galaxy clusters deflect light from background sources, which is observed in the form of image distortions (Lynds & Petrosian, 1986). This is known as the gravitational lensing effect. These mass concentrations act as lenses, where interestingly, the phenomenon demonstrates the influence of dark matter as gravity bends the light of distant cluster-member galaxies.

The two forms of the gravitational lensing effect include strong and weak lensing, which depend on the level of image distortions produced (Bartelmann, 2010). In strong lensing, the dense central region of the lens is aligned with the line of sight, making the light from the background source reach the observer along different paths. The strong image distortions appear as multiple images of one source and rings around the lens (Bartelmann, 2010). On the other hand, weak lensing occurs when the lens is relatively distant from the line of sight between the observer and the background sources. Image distortions in this form are mild, with arcs centred on the lens centre (Bartelmann, 2010).

Gravitational lensing is a powerful tool for probing clustering in the Universe and has also been useful in magnifying distant objects (Bellagamba et al., 2016). For example, Bayliss et al. (2020) proved that the effect could be observed in multiwavelength astronomy. With the help of optical observations, they detected a background galaxy at redshift $z = 1.5$. This makes gravitational lensing an effective technique for observing objects in the early Universe.

1.1.3 Cluster Mass Determination

One of the exciting properties of galaxy clusters is their total masses. Zwicky (1933) determined that the velocity dispersion in the Coma cluster is higher than that observed with only the visible matter concerned. He determined this result by using two methods: measuring the mass of the Coma cluster using the velocities of the galaxies and measuring the mass-to-light ratio. The ratio was surprisingly high and led him to conclude that there is "extra" matter present that does not emit light. This is known as dark matter. The cluster mass profiles enable the determination of the evolution and amount of dark matter in the Universe (Allen et al., 2011). That is, we can

Figure 1.2: Left to Right: X-ray, optical and mm wavelength images of Abell 1835. The images are centred around the X-ray peak on the same scale. Credit: Allen et al. (2011).

determine the evolution of the cluster mass, therefore dark matter, in various epochs. We discuss several combinations of techniques for determining cluster masses.

1.1.3.1 X-ray Masses

Cluster X-ray properties can be used to determine cluster masses. Assuming that the gas is in hydrostatic equilibrium with the gravitational potential and a spherically symmetric system, the cluster mass can be obtained from the density and temperature of the gas via (Fabricant et al., 1980):

$$M(r) = -\frac{rkT(r)}{G\mu m_p}\left[\frac{d\ln n}{d\ln r} + \frac{d\ln T}{d\ln r}\right], \tag{1.10}$$

where $M(r)$ is the cluster mass within radius r, $T(r)$ is the ICM temperature, G is Newton's constant, μ is the mean atomic weight, m_p is the mass of the proton, and $n = \rho/(\mu m_p)$ is the gas particle density. An additional assumption for obtaining Eq. 1.10 is assuming that the ICM follows the ideal gas law, $P = \frac{\rho kT}{\mu m_p} = nkT$. The gas density is measured from the surface brightness profile of a cluster while the ICM temperature is estimated from the spectrum continuum intensity (Ettori et al., 2013).

The reliability of the X-ray mass estimation is tested using mock X-ray observations from cosmological simulations (Rasia et al., 2012; Ettori et al., 2013). These simulations have revealed that the X-ray masses are biased low by $\sim$10$-$20% when considering the assumptions leading

to Eq. 1.10. This X-ray mass bias is due to the hydrostatic assumption being invalidated in systems with merger events or central regions of relaxed clusters where AGN feedback is usually observed (Allen et al., 2011). In Planck surveys, this bias is accounted for by multiplying the so-called hydrostatic-mass-bias factor $(1 - b)$ with the true masses obtained through simulations (Planck Collaboration et al., 2014, 2020). The factor is strongly constrained by cluster mass estimates from weak gravitational lensing, which we discuss below.

1.1.3.2 Sunyaev-Zel'dovich Masses

The SZ-effect has emerged as a promising tool for obtaining cluster masses (Carlstrom et al., 2002). This is because simulations have demonstrated a tight correlation between the cluster mass and the observable Compton Y parameter. This is a parameter defined as y (see Eq. 1.9) integrated over some region of the sky:

$$Y = \int y \, d\Omega. \tag{1.11}$$

The scaling relation ${Y_{500}}^{4} - M_{500}$ is used in Planck catalogues to determine the total cluster mass (Planck Collaboration et al., 2014). Nevertheless, the relation is calibrated using the hydrostatic equilibrium (see Eq. 1.10) or gravitational lensing observations.

For example, El Gordo was detected at redshift $z = 0.87$ through the SZ-effect (Menanteau et al., 2012; Lindner et al., 2014; Botteon et al., 2016b). Using the SZ-effect with X-ray and velocity dispersion, its mass was determined to be $M_{500} \approx 1.17 \times 10^{15}$ $M_{\odot}$, making it the most massive cluster known to date.

1.1.3.3 Weak-Lensing Masses

Gravitational lensing is considered the best technique for probing the total mass distribution projected along the line of sight, regardless of the dynamical state of the cluster (Bartelmann, 2010; González et al., 2020). Weak gravitational lensing lacks resolution at the cluster core but can be extended to study the cluster outskirts (Hoekstra et al., 2013). Although the weak lensing

[4] Compton Y parameter within R_{500}

signal can get compromised by foreground sources, the measurement of the subtle distortions can be used to determine the estimate of the projected mass. One way is done by constraining the projected mass within an aperture and an angular radius of θ_r via:

$$M(\theta_r) = \frac{c^2}{4G}\frac{D_L D_S}{D_{LS}}\theta_r^2 \zeta(\theta_r), \tag{1.12}$$

where c is the speed of light, $\zeta(\theta_r)$ represents the model for the image distortions observed, D_L, D_S and D_{LS} are the distances between the observer and lens, the observer and source, and the lens and source, respectively.

Weak-lensing mass estimates are compared with numerical simulations. Using weak-lensing and X-ray mass estimates from simulations, Meneghetti et al. (2010) revealed that comparisons using individual clusters are limited due to the three-dimensional nature of DMHs. Hence, this is accounted for by combining multiwavelength data (Limousin et al., 2013). Weak lensing mass estimates have been used to constrain masses in the Planck surveys (Planck Collaboration et al., 2014, 2020).

1.2 Diffuse Radio Emission

Radio observations reveal a variety of cluster sources. Following the classification from van Weeren et al. (2019), they consist of giant radio halos, mini-halos, radio relics and the revived AGN fossil plasma. We will describe them in detail in the following sections.

1.2.1 Radio Halos

Radio halos are centrally-located, unpolarised, diffuse radio sources with typical Mpc sizes, mostly found in dynamically disturbed galaxies (Brunetti & Jones, 2014; van Weeren et al., 2019). They never show an optical counterpart. The prototype of radio halos is found in the Coma cluster with a size of $\sim$2 Mpc (Large et al., 1959; Bonafede et al., 2022). A classic example of a radio halo is shown in Fig. 1.3.

The morphology of radio halos is generally regular and smooth, and the radio emission approximately follows the X-ray morphology (van Weeren et al., 2019). The azimuthally-averaged

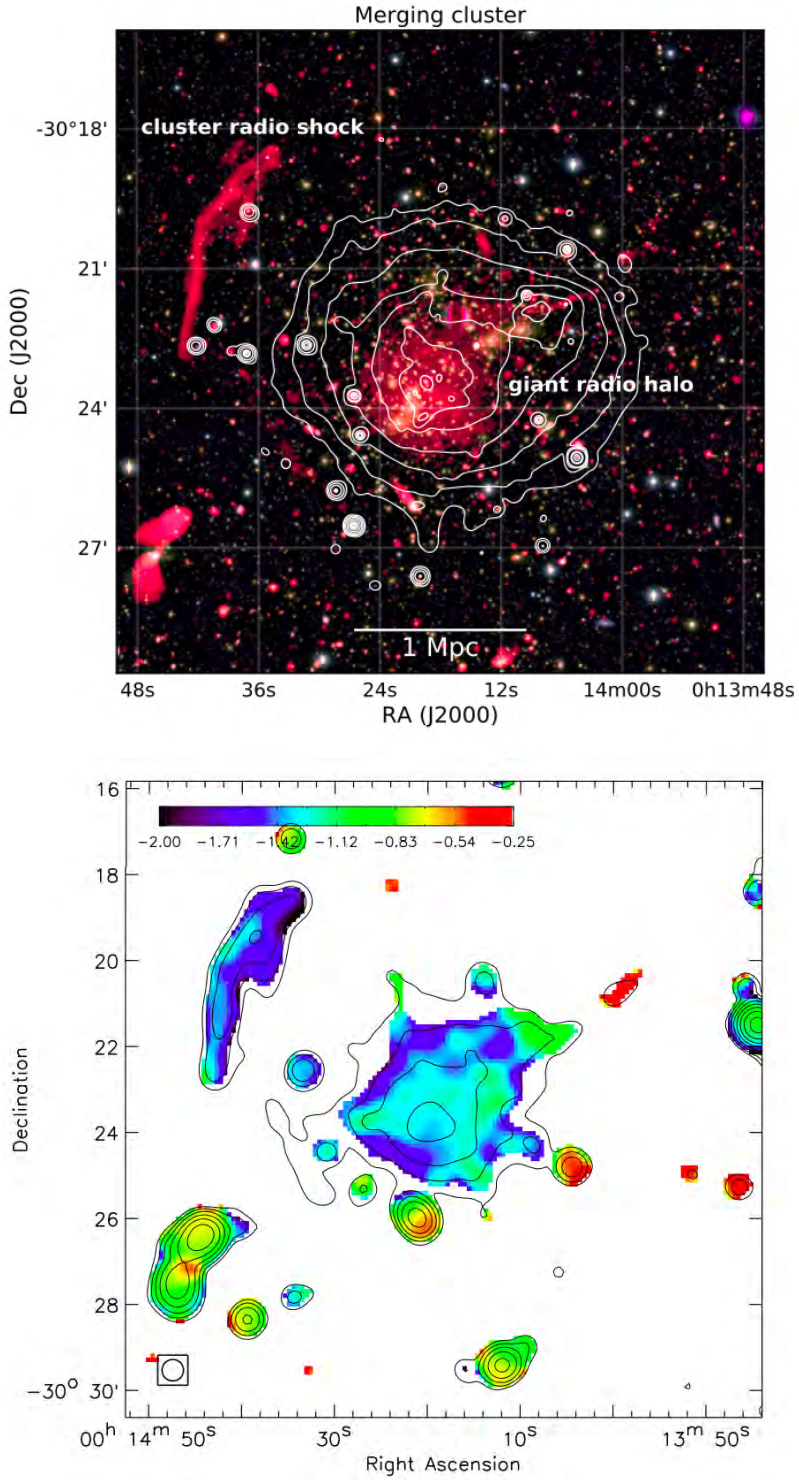

Figure 1.3: Top: 1.5 GHz image of the radio halo in Abell 2744. White contours are from X-ray observations (van Weeren et al., 2019). Bottom: Radio contours overlaid on the spectral index map between 1.5 and 3 GHz. Contours are drawn at [1, 2, 4, 8,...]$\times 3\sigma$, where σ is the rms noise (Pearce et al., 2017).

brightness profile $I(r)$ can be reasonably fit with an exponential form (Murgia et al., 2009):

$$I(r) = I_0\, e^{-r/r_e}, \tag{1.13}$$

where I_0 and r_e are free parameters defined as the central surface brightness and radius at which the brightness drops to I_0/e, respectively. Bonafede et al. (2017) determined the median value of R_H/r_e as 2.6, where R_H is the measure of the radio halo radius estimated from images and explicitly calculated as $R_H = \sqrt{R_{min} \times R_{max}}$ (Cassano et al., 2007) – R_{min} and R_{max} are the minimum and maximum radii of the 3σ level contour.

Radio halos have 1.4-GHz powers ranging between 10^{22} and 10^{26} W Hz^{-1} (van Weeren et al., 2019). The most powerful radio halo recorded to date is found in the MACS J0717.5+3745 cluster, with a radio power of $P_{1.4\ \mathrm{GHz}} \approx 1.6{\times}10^{26}$ W Hz^{-1} (Bonafede et al., 2009; van Weeren et al., 2009). The least powerful is hosted by PSZ2G145.92-12.53, with a power of $P_{1.4\mathrm{GHz}} \approx 2{\times}10^{22}$ W Hz^{-1} (Botteon et al., 2021).

Radio halos are not ubiquitous but are only found in a fraction of clusters. Early studies tried to establish a correlation between radio power and X-ray luminosity, finding that radio halos are present in $27\% - 44\%$ of X-ray luminous clusters, i.e. $L_X > 10^{45}$ erg s^{-1} (Giovannini et al., 1999). In the $z = 0.3 - 0.6$, the fraction grows up to 71% when considering clusters with disturbed X-ray morphology (Giovannini et al., 2020).

More recently, the correlation between radio power and mass has been adopted more widely, as the cluster mass is a more physical parameter compared to X-ray luminosity. The radio-halo occurrence for massive clusters ($M_{500} \geq 8 \times 10^{14}$ M$_\odot$) is fairly high ($\sim$ 70%) whereas it drops at lower masses to $\sim$ 35% (Cuciti et al., 2021b).

Initial surveys focused mostly on the low- and medium-redshift range ($z = 0.2 - 0.4$ Kale et al., 2013, 2015). The advent of the LOFAR Two-metre Sky Survey (LoTSS) has extended the cluster sample size (Hoang et al., 2022) as well as the redshift range (Cassano et al., 2019; Botteon et al., 2022). In particular, Di Gennaro et al. (2021a) identified a sample of 19 clusters at $z > 0.6$ in the LoTSS survey, finding a somewhat surprising $\sim 50\%$ radio halo occurrence.

1.2.1.1 Origin of Radio Halos

The typical crossing time of a halo size is larger than the radiative particle life time (i.e. the time necessary for a particle to lose energy due to synchrotron radiation), therefore, the presence of radio halos requires a form of in-situ particle acceleration. Two competing models have been proposed to explain the origin of radio halos. In the hadronic model, the radio emission is due to hadronic interactions between relativistic protons and ICM protons (Dennison, 1980; Blasi & Colafrancesco, 1999). Since the relativistic protons are inefficient in losing energy and diffusing for cosmological timescale, they then build up and populate the cluster halo. In the competing model, radio halos form through the turbulent re-acceleration of seed electrons induced by cluster mergers (Brunetti et al., 2001; Petrosian, 2001).

The hadronic model is currently largely disfavoured by the lack of γ-ray emission in galaxy clusters. The emission is expected as a consequence of the decay of neutral pions due to proton-proton interactions (Pinzke et al., 2011). The lack of γ-ray emission from the Coma cluster excludes the hadronic origin of its prototypical radio halo almost independently of the magnetic field intensity (Brunetti et al., 2017).

Currently, the turbulent re-acceleration model is generally accepted as the main mechanism for generating radio halos. In particular, it can connect the radio-halo occurrence with the cluster merger history or dynamic state (Cassano & Brunetti, 2005), supported by several observations (Cassano et al., 2013; Cuciti et al., 2015; Giovannini et al., 2020). In addition, the turbulent re-acceleration scenario predicts ultra-steep spectrum radio halos (Cassano, 2010), confirmed by recent low-frequency observations (Cuciti et al., 2021a,b).

1.2.1.2 Spectral Index Properties

The integrated spectral indices of radio halos are mostly in the $-1.4 < \alpha < -1$ range (Giovannini et al., 2009; Di Gennaro et al., 2021b), with a typical value of -1.3 (Feretti et al., 2012). A recent study by Rajpurohit, K. et al. (2021) determined that the integrated spectrum of the radio halo in MACS J0717.5+3745 cannot be described by a single power-law spectrum. Instead, there is spectral steeping above 1.5 GHz frequencies. They suggested that this may be due to

the IC losses as the cluster is distant ($z = 0.55$). However, the nearby Coma cluster has this high-frequency steepening, which is still subject to debate (Bonafede et al., 2022).

Some halos have an ultra-steep spectrum, i.e. $\alpha \lesssim -1.6$. The prototypical ultra-steep radio halo (USSRH) is probably A 512, discovered with a spectral index of $\alpha \sim -2.1$ (Brunetti et al., 2008). These sources are subject to a frequency cutoff (ν_b) which predicts that the radio halo becomes steep when viewed at frequencies close to or beyond the cutoff (Cassano & Brunetti, 2005; van Weeren et al., 2019). In the turbulent re-acceleration model, ν_b scales as:

$$\nu_b \propto \left(1 + \frac{\Delta M}{M}\right)^3, \tag{1.14}$$

where M and ΔM are the masses of the main cluster and the subcluster in a merger event. Eq. 1.14 shows that we can expect to detect more USSRHs in systems with less energetic merger events using low-frequency and sensitive observations (van Weeren et al., 2019).

Spatially-resolved spectral index maps of radio halos can provide an understanding of their association with merger events and origin. In the case of the turbulent re-acceleration scenario, variations in the spectral index should be associated with the turbulent energy and magnetic field strength (Orrù et al., 2007). We show an example of the spatial distribution of spectral index across a radio halo in the bottom panel of Fig. 1.3. It shows that the spectral index is relatively uniform, with some patches of steep values towards its boundary. The possible uniformity suggests that the turbulent energy does not significantly change in the region.

1.2.1.3 Scaling Relations

A correlation between the 1.4 GHz radio halo power and the cluster mass within R_{500} exists (Cassano et al., 2007; Martinez Aviles et al., 2018; Cuciti et al., 2021b). We show an example of the correlation in Fig. 1.4. The grey arrows represent upper limits on the radio power of the cluster-scale emission for clusters with no diffuse emission detected. Cassano et al. (2013) determined a steep correlation of $P_{1.4\,\mathrm{GHz}} \propto M_{500}^{3.77}$. The relationship explains the high fraction of radio halos in massive clusters and indicates that cluster mass is a necessary property to consider in the radio-halo formation models.

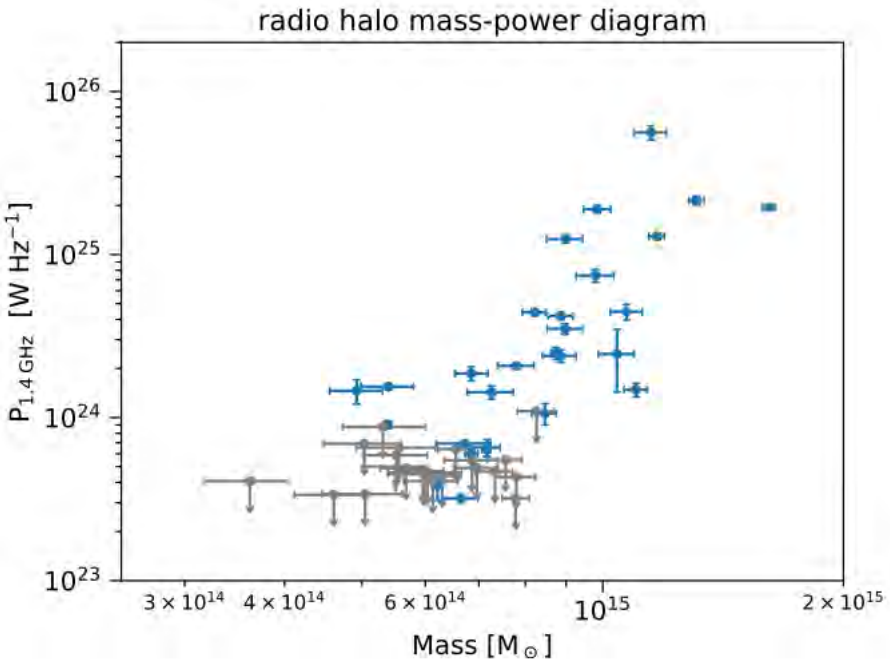

Figure 1.4: Distributions of galaxy clusters in the $P_{1.4\,\mathrm{GHz}} - M_{500}$ plane. The blue dots are clusters hosting radio halos, and the grey arrows show the upper limits. Source: van Weeren et al. (2019).

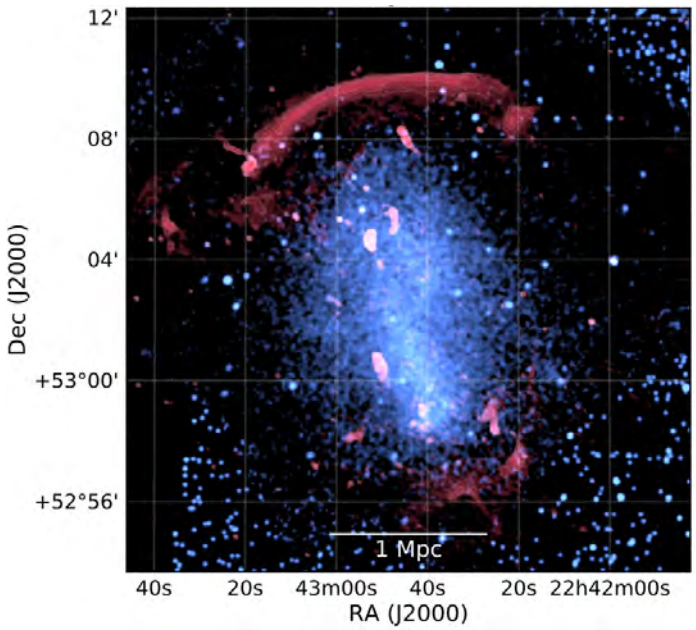

Figure 1.5: Symmetrical double radio relics in the Sausage cluster (red colour) together with the X-ray emission (blue colour; van Weeren et al., 2019).

1.2.2 Radio Relics

Radio relics are diffuse sources, generally located at the periphery of clusters with an elongated, arc-like shape extending, in some cases, up to $\sim$ 2 Mpc (see, for example, Fig. 1.3). They are generally polarized, reaching a fraction of $\sim 20 - 30\%$ at 1.4 GHz. The prototype of this class is hosted by the Coma cluster and extends over ~ 1.1 Mpc (Giovannini et al., 1985, 1991; Bonafede et al., 2022). In some interesting cases, symmetric double relics are found (see Fig. 1.5 van Weeren et al., 2011).

Interestingly, the cluster that hosts the most powerful radio halo, i.e. MACS J0717.5+3745, hosts the most powerful relic with a polarization fraction $> 30\%$ (Bonafede et al., 2009; van Weeren et al., 2009; Rajpurohit, K. et al., 2021). It has a 1.4-GHz power of $\sim 2.2\times10^{25}$ W Hz^{-1}, where its complex morphology reveals a size of $\sim$ 850 kpc with a $\alpha \approx -1.16$ spectral index. The least powerful radio relic is hosted by the merger system A 2108, with radio power of $\sim 10^{22}$ W Hz^{-1} (Schellenberger et al., 2022). It has an exceptionally steep spectral index $\alpha = -2$ at low frequencies (120$-$750 MHz) with a bent morphology (Schellenberger et al., 2022).

Although shocks are expected to be frequent events in the formation of the large-scale structure (e.g., Vazza et al., 2009), relics are a fairly rare phenomenon, appearing only in $\sim 10\%$ of the clusters observed to date (Cuciti et al., 2021a; Botteon et al., 2022). This may be due to selection effects, as detecting relics also depends on the orientation of the merger axis. That is, if the merger axis is near or in the plane of the sky, it is easy to detect relics (e.g., Golovich et al., 2019).

Fewer relics are seen in high-redshift clusters (Giovannini et al., 2020) with the furthest relic found in El Gordo (Menanteau et al., 2012; Lindner et al., 2014; Botteon et al., 2016b). The rarity at high redshifts may suggest that the number of previous mergers was not significantly large to create relics at cluster outskirts. However, it could also be brightness dimming and IC losses at these epochs (Giovannini et al., 2020). Deep radio observations are necessary to explore these suggestions.

1.2.2.1 Origin of Radio Relics

The formation of relics is not well-understood. Although, observations reveal a connection between shock fronts originating in merging clusters and relics, where particles are believed to be accelerated through either diffusive shock acceleration (DSA; Enßlin et al., 1998) or adiabatic compression (Enßlin & Brüggen, 2002).

In the DSA, particles gain energy as they are scattered by plasma irregularities downstream and upstream of the shock front, which they repeatedly cross. The energy spectrum of the electron population accelerated by DSA follows a power-law distribution via:

$$N(E) \propto E^{-\alpha_{\rm inj}}, \tag{1.15}$$

where $\alpha_{\rm inj}$ is the radio injection spectrum which is related to the Mach number $\mathcal{M}$ via:

$$\alpha_{\rm inj} = -\frac{1}{2}\left(\frac{\mathcal{M}^2+3}{\mathcal{M}^2-1}\right). \tag{1.16}$$

Radio relics probe particle acceleration at weaker shocks ($\mathcal{M} \lesssim 3-5$), where the DSA is inefficient because of the large acceleration efficiencies required to produce the radio relic luminosity in observations (Kang et al., 2002; Botteon et al., 2016a). Hence, theoretical models assume that

relics form in media with pre-existing relativistic particles possibly produced by the turbulent acceleration in mergers (Kang & Ryu, 2011). In this case, the DSA re-accelerates the relativistic particles resulting in synchrotron emission behind the shock. Observations show a discrepancy between Mach numbers derived from X-ray and radio observations, $\mathcal{M}_{\rm radio} > \mathcal{M}_{\rm X-ray}$, likely due to an underestimate of the X-ray Mach numbers as a result of unfavourable viewing angles and complex structures of the shock. This may challenge the DSA theory in cluster shocks.

The adiabatic compression scenario involves the constriction of a radio bubble (or lobe) of "old" relativistic plasma (Enßlin & Gopal-Krishna, 2001; Enßlin & Brüggen, 2002). AGN jets may inject relativistic plasma into the ICM, and when they turn off, the plasma in the radio lobes undergoes radiative losses. A shock wave compresses the plasma adiabatically and accelerates particles in the bubble. In this case, the compression enables relativistic electrons to regain energy and emit synchrotron radiation. This scenario is proposed due to the sound speed within the radio lobe being much higher than the velocity of shock wave (Enßlin & Brüggen, 2002), resulting in the compression of the lobe, where the energy gained and the presence of magnetic fields cause the bubble to emit radio waves.

However, the model suffers a limitation. It applies if the plasma is confined in the cloud to keep the sound speed close to the speed of light (Enßlin & Gopal-Krishna, 2001). When the plasma interacts with the surrounding ICM, the speed in the lobe drops, leading to the re-acceleration of particles governed by the DSA. Simulations have revealed that adiabatic compression can explain the elongated morphology of relics as the radio emission is confined to a narrow region behind the shock (Zhang et al., 2019). This model could also explain the rarity of relics since it requires shock waves and radio plasma that has not aged too much (0.2−2 Gyr; Enßlin & Gopal-Krishna, 2001).

1.2.2.2 Spectral Index Properties

Radio relics have integrated spectra in the $-1.0 > \alpha > -1.5$ range (Feretti et al., 2012; van Weeren et al., 2019). Given their position, it is easy to observe relics in different frequencies due to low confusing sources at this location, thus making it easy to determine spectral indices. The

integrated spectral index can be used to determine the Mach number $\mathcal{M}$ as it is related to the radio injection spectrum via:

$$\alpha = \alpha_{\rm inj} - 0.5 = -\frac{\mathcal{M}^2 + 1}{\mathcal{M}^2 - 1}. \tag{1.17}$$

Observations show that most relics have Mach numbers in the $3 - 5$ range.

1.2.2.3 Scaling Relations

Similar to radio halos, observations of relics provide the means to investigate scaling relations with cluster properties. Various correlations exist. These include the correlation between the relic 1.4-GHz radio power and cluster X-ray luminosity along with the correlation between the distance from the cluster centre to the relic and its largest linear size (LLS; Bonafede et al., 2012; de Gasperin et al., 2014).

The $P_{1.4\,\rm GHz} - L_X$ correlation possibly reflects a relationship between the X-ray luminosity and cluster mass (Pratt et al., 2009). This is because the X-ray luminosity is a mass proxy. For example, de Gasperin et al. (2014) found a correlation where $P_{1.4\,\rm GHz} \propto M_{500}^{2.83}$. This indicates that relics are likely to be found in massive clusters. However, biases may be introduced by the X-ray mass measurements (see discussion in Sec. 1.1.3).

In the case of the LLS−distance correlation, it follows the prediction that shocks are larger in the periphery of clusters. Nevertheless, this correlation may be affected by projection effects, which Bonafede et al. (2012) attempted to overcome by selecting clusters hosting double relics as they are possible results of mergers seen in the plane of the sky. This method led de Gasperin et al. (2014) to confirm the correlation. In addition to the LLS-distance correlation, they found that the relic radio power correlates with the LLS, i.e. powerful relics tend to have larger linear sizes.

1.3 Thesis Motivation

Di Gennaro et al. (2021a) observed a sample of 19 clusters at $z > 0.6$ and $M_{500} \sim 4{-}8{\times}10^{14}\,{\rm M}_{\odot}$ with a 50% radio halo occurrence. Cuciti et al. (2021a) observed a sample of 75 clusters with

mass $\mathrm{M} > 6 \times 10^{14}$ $\mathrm{M}_{\odot}$ in the $0.08 < z < 0.33$ range. They found a 70% radio halo occurrence for clusters with $M_{500} \geq 8 \times 10^{14}$ $\mathrm{M}_{\odot}$ with the fraction dropping down to 35% in less massive systems. These results provide important, supporting evidence for the turbulent re-acceleration model (Cassano & Brunetti, 2005).

An important test of the turbulent re-acceleration model is provided by the redshift evolution of the radio-halo occurrence. At high redshift, an increasing fraction of the merger energy that accelerates particles and generates radio halos is radiated away via IC losses. The fraction of radio halos in high-redshift galaxy clusters is therefore expected to be lower compared to low-redshift systems (Cassano et al., 2006). The ability to observe radio halos in high-redshift systems depends, however, on the observing frequency. In the presence of significant IC losses, the synchrotron luminosity decreases by a factor B^2/B^2_{CMB}[5], leading to a maximum synchrotron frequency emitted by the relativistic particles that scales as $\nu_s \propto B/B^2_{\mathrm{CMB}}$ (Cassano et al., 2006). This implies that, given a magnetic field value, observations carried out at frequencies $\nu > \nu_s$ will unlikely detect radio halos. Another way of saying this is that high-frequency radio surveys will likely detect only radio halos that host strong magnetic fields. Observations of high-redshift clusters can, therefore, test predictions of the turbulent re-acceleration and study the evolution of magnetic fields on cluster scales.

Until a few years ago, observations of high-redshift systems were fairly rare and focused on peculiar systems. However, the advent of low-frequency follow-up of SZ-selected cluster surveys is quickly changing the landscape. Knowles et al. (2019) found only one radio halo in a sample of 14 clusters at $z > 0.5$ with $\mathrm{M} > 5 \times 10^{14}$ $\mathrm{M}_{\odot}$, observed at 610 MHz. Observations at ~ 140 MHz pushed the search up to $z \sim 0.9$, finding an occurrence rate similar to low-redshift systems, requiring, therefore, mechanisms of early amplification of magnetic fields on cluster scales (Cassano et al., 2019; Di Gennaro et al., 2021a,b).

When moving up to GHz frequencies, the turbulent re-acceleration model predicts a radio-halo occurrence rate of a few % at $M_{500} \sim 6 \times 10^{14}$ $\mathrm{M}_{\odot}$, increasing up to $\sim 10\%$ for $M_{500} \sim 10^{15}$ $\mathrm{M}_{\odot}$ (Cassano et al., 2006). If they follow the radio halo power vs cluster mass correlation

[5] B_{CMB} is the magnetic field corresponding to the CMB energy at the cluster redshift.

and using the best-fit values from Cuciti et al. (2021b), their power would fall in the $0.8 - 5.8 \times 10^{24}$ W Hz^{-1} range.

In this thesis, we present MeerKAT observations of three moderately high-redshift clusters ($0.42 \lesssim z \lesssim 0.46$) with masses in the $6 - 10 \times 10^{14}$ M$_{\odot}$ range, selected because of their highly disturbed dynamical state. Our work will test expectations of the turbulent re-acceleration model and investigate the magnetic field properties in a somewhat little explored redshift range.

The remainder of the thesis is organised as follows: In Chapter 2, we briefly introduce radio interferometry, our data observations and reduction steps. In Chapter 3, we introduce various quantities for our analysis and provide the analysis and results. We then produce the discussion and conclusions in Chapter 4.

Throughout the thesis, we use a flat cosmology with $H_0 = 70$ km s^{-1} Mpc^{-1}, $\Omega_{\rm M} = 0.3$, and $\Omega_{\Lambda} = 0.7$.

CHAPTER 2

Observations and Data Reduction

In this chapter, we review radio interferometry, the pioneering work from its foundation and current progress. We introduce the MeerKAT telescope and describe our observations, and data reduction techniques.

2.1 Introduction to Radio Interferometry

During the early 1930s, Karl G. Jansky made a radio-wave detection using an antenna he had built to study the noise of radio receivers (Jansky, 1932). He later determined that the origin of the excess noise he measured was an astronomical radio source from the direction of the Milky Way centre (Jansky, 1935). This discovery was the first step for radio astronomy which, at the time, did not develop further until Grote Reber built the first single-dish radio telescope for astronomy (Reber, 1940, 1942). This paved the way for astronomical observations in different parts of the electromagnetic spectrum.

I will follow the treatment from the interferometry book by Thompson et al. (2017). The flux density S_ν of a radio source is defined as the energy of radiation received per unit time, per unit

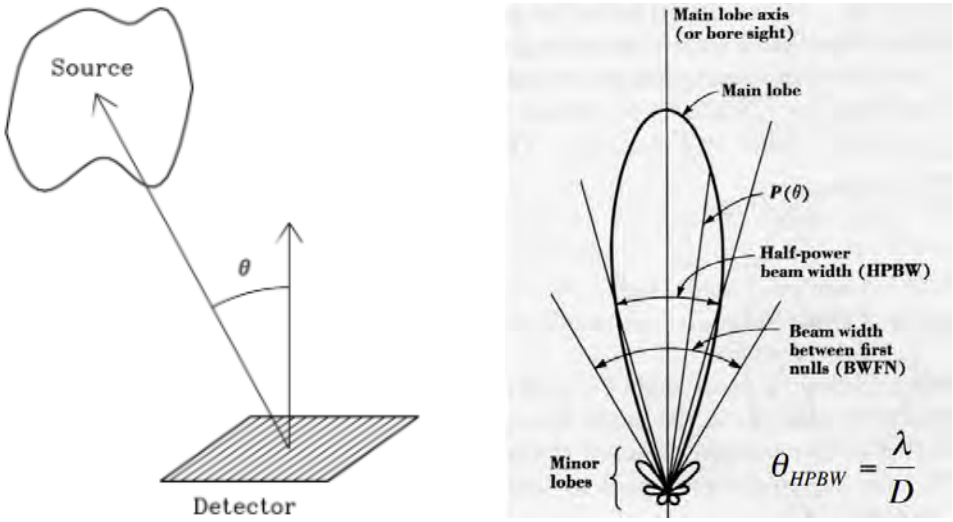

Figure 2.1: Left: Schematic representation of the geometry of incoming radiation on a detector. The angle θ is measured between the detector plane and the source radiation direction (Condon & Ransom, 2016). Right: Example of antenna primary beam pattern (Kraus, 1986)

area and per frequency interval at the frequency ν:

$$S_\nu = \int_\Omega I_\nu(\Omega') \cos\theta \, \mathrm{d}\Omega', \tag{2.1}$$

where Ω is the solid angle subtended by the source, θ is the angle between the line of sight and the detector plane (see left image Fig. 2.1), and I_ν is the brightness of the source at the observing frequency. The brightness temperature T_b is the temperature that a black-body would have, to produce the same brightness as the observed source, i.e. $I_\nu = B_\nu(T_b)$. The specific intensity B_ν is given by Planck's law:

$$B_\nu(T) = \frac{2kT\nu^2}{c^2} \left[\frac{h\nu/kT}{e^{h\nu/kT} - 1} \right], \tag{2.2}$$

where h is the Planck constant and c is the speed of light. The Rayleigh-Jeans approximation, where $h\nu << kT$ is often adopted at radio wavelengths, and Eq. 2.2 then becomes:

$$B_\nu(T) = \frac{2\nu^2 kT}{c^2}. \tag{2.3}$$

Eq. 2.3 allows us to then define the brightness temperature as:

$$T_b = \frac{c^2}{2\nu^2 k} I_\nu. \tag{2.4}$$

Antennas are detectors commonly adopted in radio observations. The antenna diameter D sets its angular resolution, i.e. the minimum distance at which two point-sources can be seen as separate:

$$\Delta\theta = 1.22\,\frac{\lambda}{D}, \tag{2.5}$$

where λ is the observing wavelength. Eq. 2.5 shows that to get greater angular resolution, we need to increase the size of the collecting area, i.e. its diameter. However, this can be expensive and infeasible. In order to improve the angular resolution, the signals coming from an array of single-dish telescopes can be combined together to synthesise a single dish with an aperture as large as the maximum separation among the array telescopes. This is known as a radio interferometric array. The first two-dish radio interferometer was built to operate at 175 MHz by Ryle & Vonberg (1946) to study radio emission from solar observations.

For simplicity, we will consider a two-element interferometer (see Fig. 2.2). The separation between two elements is called a baseline, where for an interferometer with N elements, there are $N(N-1)/2$ baselines. The key concept is that the incoming radiation reaches the two antennas at different times, i.e. with a geometric delay τ_g of the form:

$$\tau_g = \frac{\vec{b}\cdot\vec{s_0}}{c}, \tag{2.6}$$

where $\vec{s_0}$ is the direction of the observed source and $\vec{b}$ is the baseline between the elements (Fig. 2.2). These signals are then multiplied and integrated in the correlator. The correlator output is called visibility, and it can be related to the brightness distribution of the sky I via the van Cittert–Zernike theorem:

$$V_{pq}(u,v) = \int_{-\infty}^{\infty}\int_{-\infty}^{\infty} I(l,m)e^{-i2\pi(ul+vm)}\mathrm{d}l\mathrm{d}m, \tag{2.7}$$

where pq identifies the two antennas p and q, (l,m) are the direction cosines given in angular units, and (u,v) are the components of the baseline as viewed from the source in wavelength units (Fig. 2.2). Components u and v are the samples of the uv-domain, which, according to Eq. 2.7, are Fourier pairs with coordinates in the image domain (lm). In modern radio telescopes, the w coordinate is non-negligible, i.e. the three-dimensional nature of the sky cannot be completely

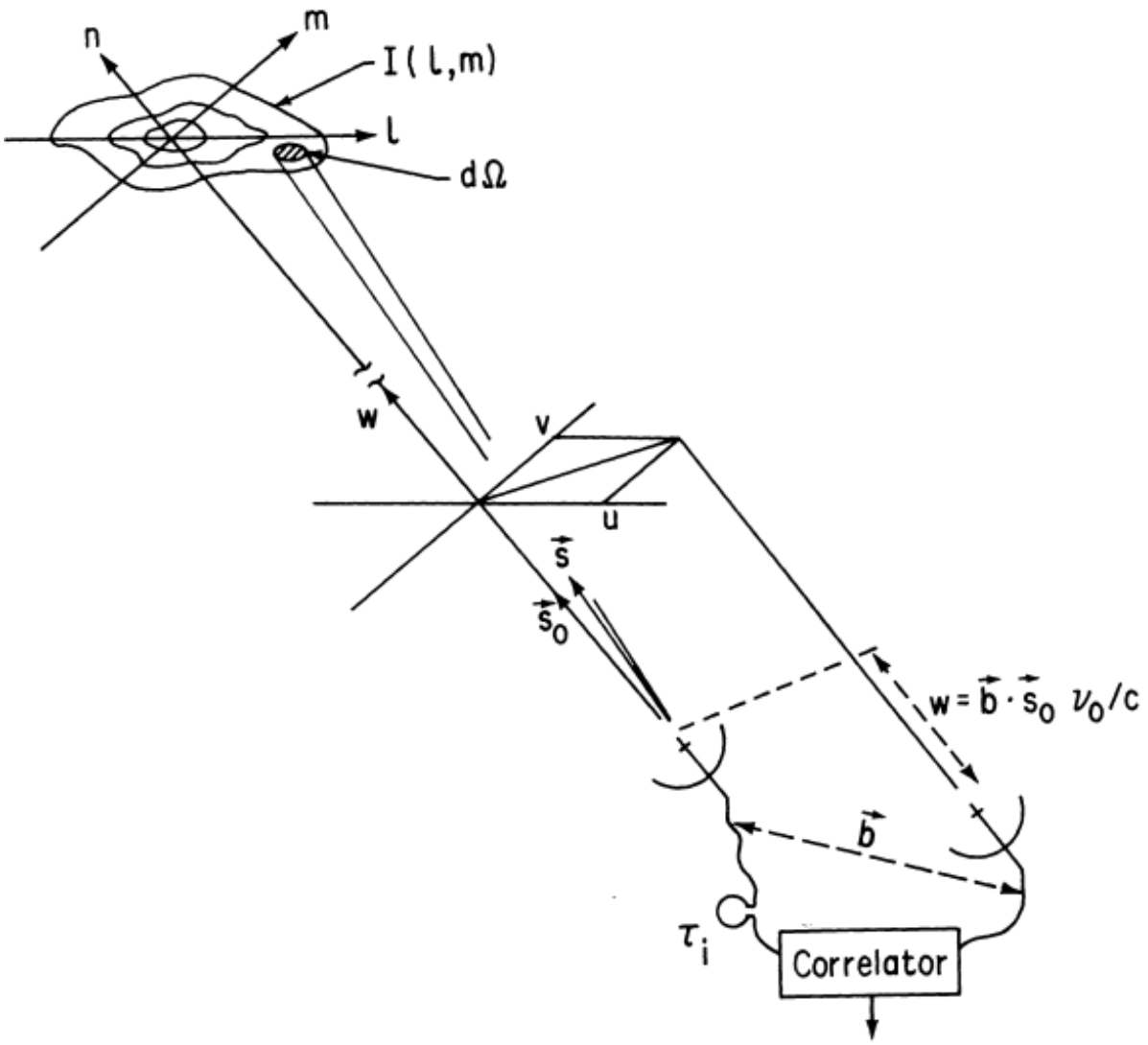

Figure 2.2: Illustrations of the two-element radio interferometer showing the antennas receiving the signals, which get correlated and the relationship between the (u, v, w) space and (l, m, n) space (Thompson, 1999). The instrumental delay τ_i compensates the geometric delay τ_g so that signals arrive at the correlator simultaneously.

ignored, and Eq. 2.7 becomes:

$$V_{pq}(u,v) = \int_{-\infty}^{\infty}\int_{-\infty}^{\infty} \frac{I(l,m)}{n} e^{-i2\pi(ul+vm+w(n-1))} \mathrm{d}l\mathrm{d}m, \tag{2.8}$$

where w is in the direction normal to the uv-domain and $n = \sqrt{1-l^2-m^2}$ is in the projection along the w-direction (see Fig. 2.2). The w-projection involves projecting the (u,v,w) visibility to the $(u,v,w=0)$ visibility. This is done by convolving the uv-samples with the appropriate w-term-correcting kernel of the corresponding (u,v,w) coordinate. Accounting for the w-term can be computationally expensive, although techniques such as the w-projection (Cornwell et al., 2008) algorithm have been introduced as solutions.

Antennas are not uniformly sensitive to radiation in all directions and are most sensitive in the direction where they are pointing. This gives a beam pattern with the main lobe pointing in the direction of interest and side lobes as responses outside this region (see right panel of Fig. 2.1 for an example).

Each baseline generates a track in the uv-plane as the Earth rotates. The ensemble of tracks generated by all baselines is called uv-coverage and represents the visibility sampling function. It can improve through accumulating samples over time, thus enhancing our knowledge of observed sources.

In the remainder of the section, I want to introduce the Radio Interferometric Measurement Equation (RIME), a powerful formalism used to describe the interferometric signal path (Hamaker et al., 1996; Smirnov, 2011). The radiation received by an antenna p induces a voltage $\mathbf{v}_p$:

$$\mathbf{v}_p = \mathbf{J}_p \mathbf{e}_p \tag{2.9}$$

where $\mathbf{J}_p$ is a 2×2 Jones matrix and $\mathbf{e}_p$ is the incident, electromagnetic field vector. A similar equation can be written for antenna q, resulting in a visibility matrix $\mathbf{V}_{pq}$:

$$\mathbf{V}_{pq} = 2\left\langle \begin{pmatrix} v_{pa} \\ v_{pb} \end{pmatrix} \begin{pmatrix} v_{qa}^* & v_{qb}^* \end{pmatrix} \right\rangle, \tag{2.10}$$

where v^* is a conjugate of v, a and b are antenna feeds, and $\langle\rangle$ represents the time average. Considering the different signal paths to antennas p and q, and assuming that $\mathbf{J}_p$ and $\mathbf{J}_q$ are

constant over the averaging interval, the visibility matrix in Eq. 2.10 can be represented as:

$$\mathbf{V}_{pq} = 2\,\mathbf{J}_p \langle ee^H \rangle\, \mathbf{J}_q^H, \tag{2.11}$$

where H is the Hermitian transpose operator. The term in the angle brackets is the source brightness matrix $\mathbf{B}$, which is expressed as:

$$\mathbf{B} = 2\langle ee^H \rangle = \begin{pmatrix} \langle e_x e_x^* \rangle & \langle e_x e_y^* \rangle \\ \langle e_y e_x^* \rangle & \langle e_y e_y^* \rangle \end{pmatrix} = \begin{pmatrix} I+Q & U+iV \\ U-iV & I-Q \end{pmatrix}, \tag{2.12}$$

where I, Q, U, and V are the Stokes parameters representing the polarization state of the source. Therefore, Eq. 2.11 and E. 2.12 lead to the basic form of the RIME:

$$\mathbf{V}_{pq} = \mathbf{J}_p\, \mathbf{B}\, \mathbf{J}_q^H. \tag{2.13}$$

The RIME is used to calibrate the observed signal and relates the observed visibility $\mathbf{V}_{pq}^{obs}$ to the true visibility $\mathbf{V}_{pq}^{true}$ of antenna p and q via:

$$\mathbf{V}_{pq}^{obs} = \mathbf{J}_p\, \mathbf{V}_{pq}^{true} \mathbf{J}_q^H, \tag{2.14}$$

When extended to emission coming from the whole sky, the RIME can be generalized as follows:

$$\mathbf{V}_{pq} = \iint\limits_{lm} \mathbf{J}_p(l,m)\, \mathbf{B}(l,m)\, \mathbf{J}_q^H(l,m)\, \frac{\mathrm{d}l\mathrm{d}m}{n}. \tag{2.15}$$

The matrices $\mathbf{J}_p$ and $\mathbf{J}_q$ can be split into direction-dependant effects (DDEs) and direction-independent effects (DIEs) associated with the antennas p and q, respectively.

DIEs are functions of frequency and time that can vary in both quantities but remain constant in different regions of the sky. Propagation effects like the time-variable receiver gain $\mathbf{G}(t)$ and frequency-variable bandpass $\mathbf{B}(\nu)$ are examples of DIEs. Both effects may be combined into one Jones matrix $\mathbf{G}'(t,\nu)$:

$$\mathbf{G}'(t,\nu) = \mathbf{G}(t) \cdot \mathbf{B}(\nu) \approx \begin{pmatrix} g_x & 0 \\ 0 & g_y \end{pmatrix} \cdot \begin{pmatrix} b_x & 0 \\ 0 & b_y \end{pmatrix}. \tag{2.16}$$

With modern radio telescopes, DDEs have become a prominent source of errors in observations. DDEs are also functions of time and frequency but include the dependency on the position in the sky.

Both DIEs and DDEs need to be corrected in order to reconstruct the sky brightness distribution. This process is called calibration

2.1.1 Conventional Calibration

The RIME in Eq. 2.14 is the form typically used for calibration. The traditional calibration technique involves the flagging of radio frequency interference (RFI), first-generation calibration (1GC) and direction-independent self-calibration (2GC). RFI is the unwanted radiation that disrupts observations, for example, signals from aeroplanes and satellites. 1GC generally uses two calibration sources to correct for DIEs. The primary calibrator is a point-like source used for the delay, bandpass and flux calibration, generally observed at the beginning of the observation. The delay calibration removes the phase delay error caused by inaccurate antenna position or timing, and the bandpass calibration corrects the errors caused by the system frequency response. The flux calibration is used to adjust and properly scale the flux density of the observed sources to a standard reference. Accurate models of sources such as 3C286, 3C147 and 3C48 are typically used for this procedure. The secondary calibrator is a relatively bright (preferably close to the target) source observed throughout the observation in order to correct time variations of the instrument gain.

Solutions from 1GC are then applied to the target field, and visibilities can be Fourier transformed into an image. Calibration accuracy is often measured through a quantity called dynamic range DR:

$$\mathrm{DR} = \frac{I_p}{\sigma_I}, \tag{2.17}$$

where I_p is the peak brightness of the image and σ_I is its root-mean-square (rms) noise. To improve the DR, we can perform 2GC to calibrate visibilities using the target field. 2GC is an iterative procedure which derives a sky model from the target field and uses the model to improve calibration solutions. Such improved calibration is expected to generate a better image (i.e. with a higher DR) which, in turn, produces a more accurate sky model that is expected to lead to an even more accurate calibration. This loop can be repeated until the process somewhat converges into a final image.

Standard calibration can be done using pipelines with set parameters in configuration files. Examples of software packages that use this procedure are, among others, the Containerized Automated Radio Astronomy CALibration (CARACAL; Józsa et al., 2020), Common Astronomy Software Applications (CASA; McMullin et al., 2007) and CUBICAL (Kenyon et al., 2018). We use these tools to reduce our MeerKAT data. See Sec. 2.2.3 for a detailed description.

2.1.2 Direction-Dependent Calibration

Sensitive, wide-field observations taken with modern radio interferometers are often plagued by DDEs and need direction-dependent calibration (3GC) in order to improve their DR (Smirnov, 2011). Various approaches to calibrate DDEs have been developed, including facet-based (Tasse et al., 2018) and peeling (Noordam, 2004) algorithms. Faceting involves approximating the wide field of view (FOV) with small narrow-field images called facets. The brightest source is tagged in each facet, and 2GC is performed on individual facets, generally leading to a DR improvement. On the other hand, peeling is an iterative process which finds the brightest source, solves for its DDEs, applies the solutions to the visibilities and subtract the source from the visibilities. It then finds the next brightest source and repeats the process. Peeling repeats until DDEs are solved for all the bright sources in the field. Software packages such as CUBICAL and KILLMS[1](Smirnov & Tasse, 2015) implement both approaches.

2.1.3 Imaging

Since a radio interferometer has a finite number of baselines, visibilities cannot sample the whole uv-domain. This is described by the sampling function $S(u, v)$, which is zero for points where there is no measurement and thus depends on the array configuration. The Fourier inversion of the visibility equation (Eq. 2.7) can be used to obtain the dirty image I_ν^D:

$$I_\nu^D = \iint V_\nu(u, v)\, S(u, v)\, e^{-2\pi i(ul+vm)}\, du\, dv = I_\nu^{true}(l, m) * B(l, m), \tag{2.18}$$

[1]https://github.com/saopicc/killMS

where $*$ is the convolution operator, I_ν^{true} is the true brightness distribution and $B(l, m)$ is the synthesised beam, also known as the array point-spread function (PSF). The PSF is the response of the radio interferometer to an ideal point source and the Fourier transform of the uv-domain sampling function, i.e. $B(l, m) \rightleftharpoons S(u, v)$.

Partial uv-coverage leads to strong sidelobes in the PSF, contaminating the dirty image. As this is the case in most existing interferometers, we use a technique called deconvolution to get a better estimate of the true sky brightness distribution. The most used deconvolution technique is the CLEAN algorithm, an iterative deconvolution method first introduced by Högbom (1974) and later advanced by Clark (1980) and Schwab (1984). The basic procedure of CLEAN is as follows:

1. Make a copy of the dirty image and name it the residual image.
2. Find the peak pixel value and its location in the residual image.
3. At this location, subtract the PSF multiplied by the peak pixel value and a gain factor γ, which sets the amount of flux subtracted.
4. Record the location and the subtracted magnitude of the point source in a model image.
5. Go back to Step 2 and iteratively repeat the procedure until either the number of iterations has reached the user-specified limit or the peak of the residual image is below the user-specified threshold.
6. Convolve the model image with a restoring beam called the CLEAN beam. It is usually chosen to be a Gaussian fit of the main lobe of the PSF.
7. Add the residual image from Step 5 to the CLEAN image in Step 6.

The CLEAN algorithm so described generally performs poorly in the presence of extended sources as it attempts to model them as a collection of independent pixel values. As a consequence, CLEAN can sometimes generate spurious structures in the restored image as it attempts to remove the point-source component of the extended source. Rau & Cornwell (2011) introduced the multiscale CLEAN to better model extended sources.

Once uv tracks are combined together in the uv-plane, visibilities measured by different baselines can be given different weights resulting in different PSFs. Common choices include natural weighting, uniform weighting and uv-taper functions. For natural weighting, each uv cell receives a weight proportional to the number of visibilities points that fall in the cell. As short baselines are sampled more often than longer ones, the resulting PSF has the largest main lobe. This choice maximizes the sensitivity at the cost of poor resolution. For uniform weighting, each uv cell position is given equal weight regardless of the number of samples that fall in it. This up-weighs longer baselines with respect to the short ones, resulting in the highest possible resolution at the cost of sensitivity. A convenient weighting scheme is the Briggs weighting (Briggs, 1995), which smoothly varies between natural and uniform weighting. It uses the robustness parameter R, which at $R = -2$, approximates uniform weighting, and at $R = 2$, it approximates natural weighting. Visibilities can also be weighted using a tapering function, normally a Gaussian profile that is a function of the uv length and is generally introduced to increase the sensitivity to extended structures while retaining a PSF with relatively low sidelobes.

2.2 Observations and Data Reduction

2.2.1 The MeerKAT Telescope

The quest to introduce observational radio interferometry in South Africa started with the seven-dish Karoo Array Telescope (KAT-7; Booth & Jonas, 2012). It was built in a low-population location in the Karoo, Northern Cape, and is a compact array with a maximum baseline of 185 m that covers a frequency range between 1.2 and 1.95 GHz. Although the goals of KAT-7 were mainly engineering-driven, it produced various science results (Carignan et al., 2013; Bernardi et al., 2016; Mhlahlo & Jamrozy, 2021).

MeerKAT is the KAT-7 successor, located near it and observes at declination $\delta < +45^{\circ}$ (see Fig. 2.3; Jonas & MeerKAT Team, 2016; Camilo et al., 2018; Mauch et al., 2020). It was inaugurated in July 2018 and is operated by the South African Radio Astronomy Observatory. MeerKAT is a precursor of the Square Kilometre Array with 64, 13.5 m diameter dishes and

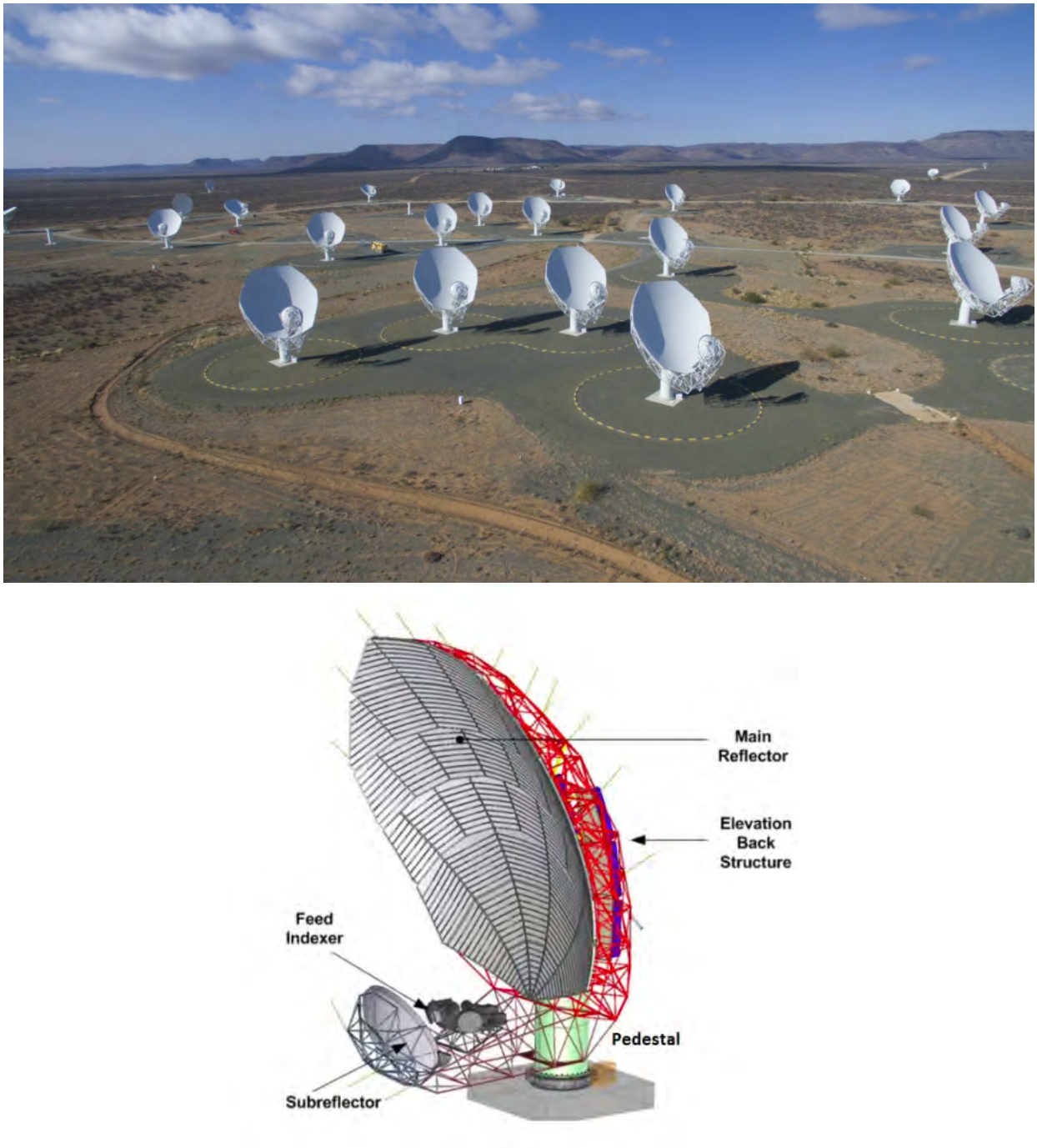

Figure 2.3: Top: picture of the MeerKAT core, Northern Cape, South Africa. Source: Square Kilometre Array Observatory. Bottom: A schematic representation of a MeerKAT antenna structure (Jonas & MeerKAT Team, 2016).

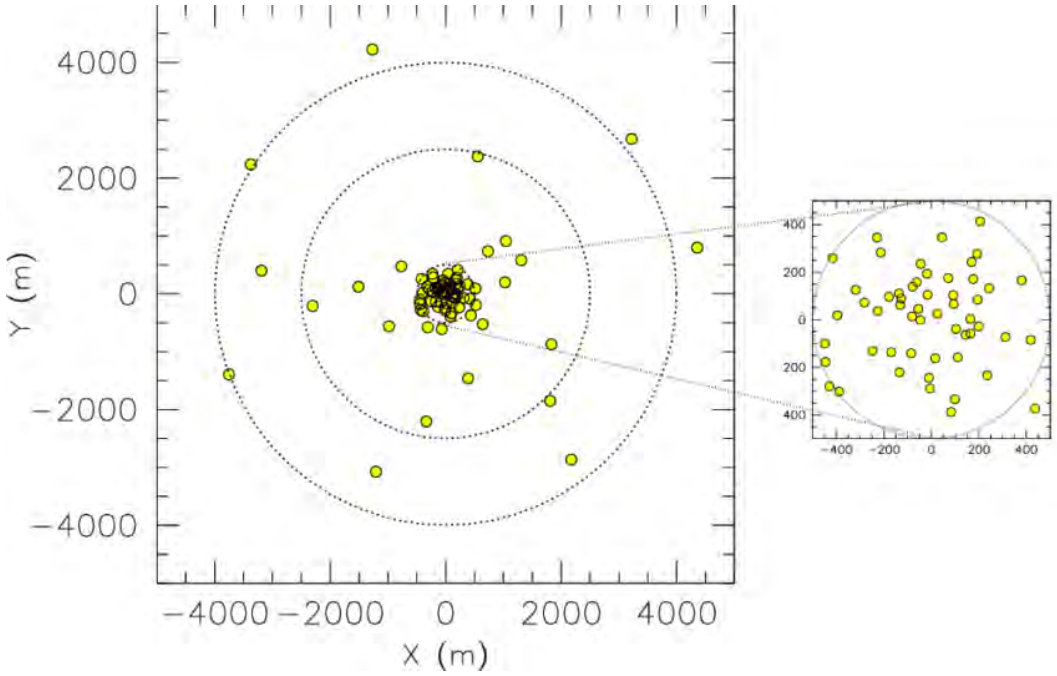

Figure 2.4: Layout of the MeerKAT array with its ∼70% antennas in the core (Booth et al., 2009).

baselines ranging from 29 m to 8 km. The maximum baseline length allows for a high resolution – up to $\sim 6.6''$ at 1.4 GHz. Approximately 70% of the 64 antennas form the MeerKAT core (see Fig. 2.4), providing a high-brightness sensitivity array. The inner core layout is a 2D Gaussian distribution in the uv-domain, and the outer core is another 2D Gaussian distribution.

The MeerKAT antennas are labelled m000 through to m063, following the distance of the antennas from the array centre. Each dish has an offset Gregorian optical layout (see Fig. 2.3) with a 3.8 m elliptical sub-reflector feed indexer positioned down to ensure that the aperture is not blocked, allowing for a high aperture efficiency and reduced RFI. This type of antenna has dual offset reflectors where the feed is off-axis to the primary reflector (Yeap et al., 2016). The cylindrical pedestal on MeerKAT antennas has a conical top section extending from the primary reflector to deflect unwanted radiation from the ground away from the feed. The foundation of each dish lies underground and was created to have the required dish pointing accuracy and for lightning protection.

A MeerKAT antenna can carry two cryogenic receivers, operating at L- (900-1670 MHz) and

Table 2.1: MeerKAT receiver bands specifications from Jonas & MeerKAT Team (2016).

Frequency Band :	UHF	L
System temperature (K)	< 27	< 22
Frequency range (MHz)	$580-1015$	$900-1670$
Total bandwidth (MHz)	435	770
Instantaneous bandwidth (MHz)	544	856

UHF-bands (Ultra high frequency; 580-1015 MHz; see Table 2.1). At L-band, the MeerKAT primary beam has a $\sim 1.2^{\circ}$ full width at half maximum and brightness sensitivity on angular scales larger than $\sim 1'$.

2.2.2 Observations of the Cluster Sample

Our MeerKAT observations include three galaxy clusters selected from the South Pole Telescope and the latest Planck Sunyaev-Zel'dovich (PSZ2; Planck Collaboration et al., 2015, 2016) catalogue as part of a pilot study that focuses on searching for radio halos in clusters at redshifts higher than previous surveys (Venturi et al., 2009; Cuciti et al., 2021a). We selected three clusters: PSZ2G254.08-58.45 (PSZ2G254), PSZ2G255.60-46.18 (PSZ2G255) and PSZ2G277.76-51.74 (PSZ2G277). They are more massive than 6×10^{14} $M_{\odot}$, with disturbed X-ray morphology and in the $0.42 \lesssim z \lesssim 0.46$ range (see Table 2.2 for the sample properties).

Each cluster was observed in a $\sim$ 2-hour exposure time with additional overheads of $\sim$30 mins for calibration observations (see Sec. 2.2.3). The exposure time is the sum of the EXPOSURE column in the MS where the data is not flagged, i.e. where the FLAG_ROW column is not set per field. Observations were obtained between the 7th and 8th of June 2019 using MeerKAT's L-band receiver with a central observing frequency of 1.28 GHz. Even with such short exposure, the uv-coverage is fairly dense due to the high number of correlated elements (Fig. 2.5).

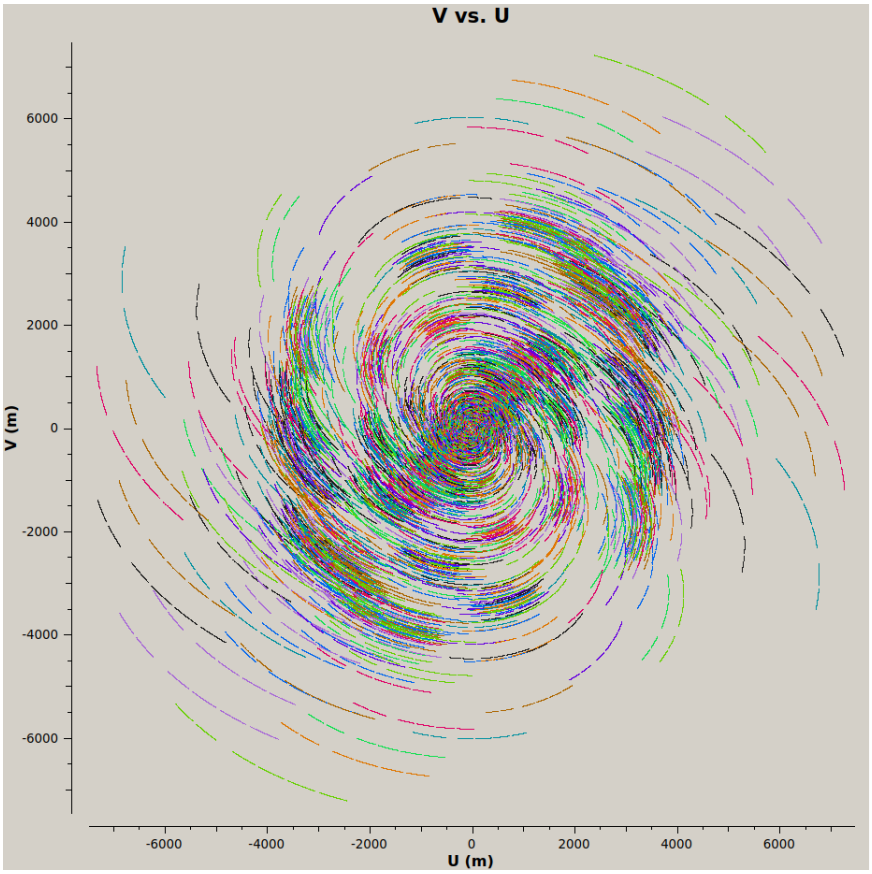

Figure 2.5: The uv-coverage corresponding to the observations of the cluster PSZ2G254. We colourised the plot based on the baselines, i.e. each pair of antennas is represented by its own colour during the observation time. Flags are not included, apart from antenna m036 which was missing across all observations. The uv-coverage is similar for the other two sources.

Table 2.2: Properties of the three target fields. Columns: (1) Name of cluster; (2)-(3) cluster redshift and centre coordinates; (4) cluster mass within R_{500} (Planck Collaboration et al., 2016); (5) scale length at the cluster redshift.

Cluster Name	z	RA (J2000)	DEC (J2000)	M_{500} ($10^{14}\mathrm{M}_{\odot}$)	Linear Scale (kpc/″)
PSZ2G254.08-58.45	0.46	$3^{\mathrm{h}}\,04^{\mathrm{m}}\,16.80^{\mathrm{s}}$	$-44^{\circ}\,01'\,51.6''$	6.2 ± 0.6	5.831
PSZ2G255.60-46.18	0.42	$4^{\mathrm{h}}\,11^{\mathrm{m}}\,15.50^{\mathrm{s}}$	$-48^{\circ}\,19'\,19.2''$	6.3 ± 0.4	5.533
PSZ2G277.76-51.74	0.44	$2^{\mathrm{h}}\,54^{\mathrm{m}}\,17.50^{\mathrm{s}}$	$-58^{\circ}\,57'\,10.8''$	9.7 ± 0.4	5.685

Table 2.3: Observational specifications. Columns: (1) cluster name; (2) secondary calibrator (3); Duration of the observations.

Cluster Name	Secondary Calibrator	Exposure time (hr)
PSZ2G254.08-58.45	J0203-4349	2.04
PSZ2G255.60-46.18	J0440-4333	2.03
PSZ2G277.76-51.74	J0303-6211	2.02

2.2.3 Data Reduction

For all our target fields, the standard primary calibrator PKS B1934-638 (Reynolds, 1994) was used for bandpass calibration, complemented by an appropriate secondary calibrator (see Table 2.3). All the observations related to each target were combined together in a single file where the integration time was averaged to 8 s from 2 s, and the number of frequency channels was reduced to 1024 (from 4096 channels) in order to speed up the processing time. Visibilities were visually inspected, and corrupted data were initially manually flagged.

After the first round of flags, we performed 1GC calibration using the CARACAL[2] pipeline. Delay, bandpass, and gain calibration were performed using PKS B1934-638 with a flux density of $S_{1.4\,\mathrm{GHz}} \sim 14.91$ Jy and $\alpha \sim -0.6$. Calibration solutions were transferred to the secondary calibrators that were used to perform delay, gain and flux-scale calibration. All calibration solutions were eventually applied to the target fields.

Visibilities for each cluster were Fourier transformed into images using WSCLEAN V2.9 (Offringa et al., 2014; Offringa & Smirnov, 2017). We used uniform weights to achieve the best angular resolution in order to generate a model of only compact sources for self-calibration. We used the CUBICAL[3] package for self-calibration. Our implementation is as follows:

1. Use the post-1GC images to create a mask with a σ threshold using BREIZORRO[4]. This is a useful software package that uses a FITS image to generate a binary mask.

2. Include the mask in the second WSCLEAN run to improve the model in the visibilities. The mask assists in the cleaning of sidelobes by probing the true emission from sources.

3. Specify the MS file with the updated model in CUBICAL

4. Execute the first cycle run to only deal with the G-Jones term parameter. With this parameter enabled, set the Jones-matrix type to solve for, as `type = f-slope`. This indicates solving for the delay and frequency-constant gain simultaneously, which is necessary due to the residual calibration errors from MeerKAT observations.

[2]https://github.com/caracal-pipeline/caracal.git
[3]https://github.com/ratt-ru/CubiCal.git
[4]https://github.com/ratt-ru/breizorro.git

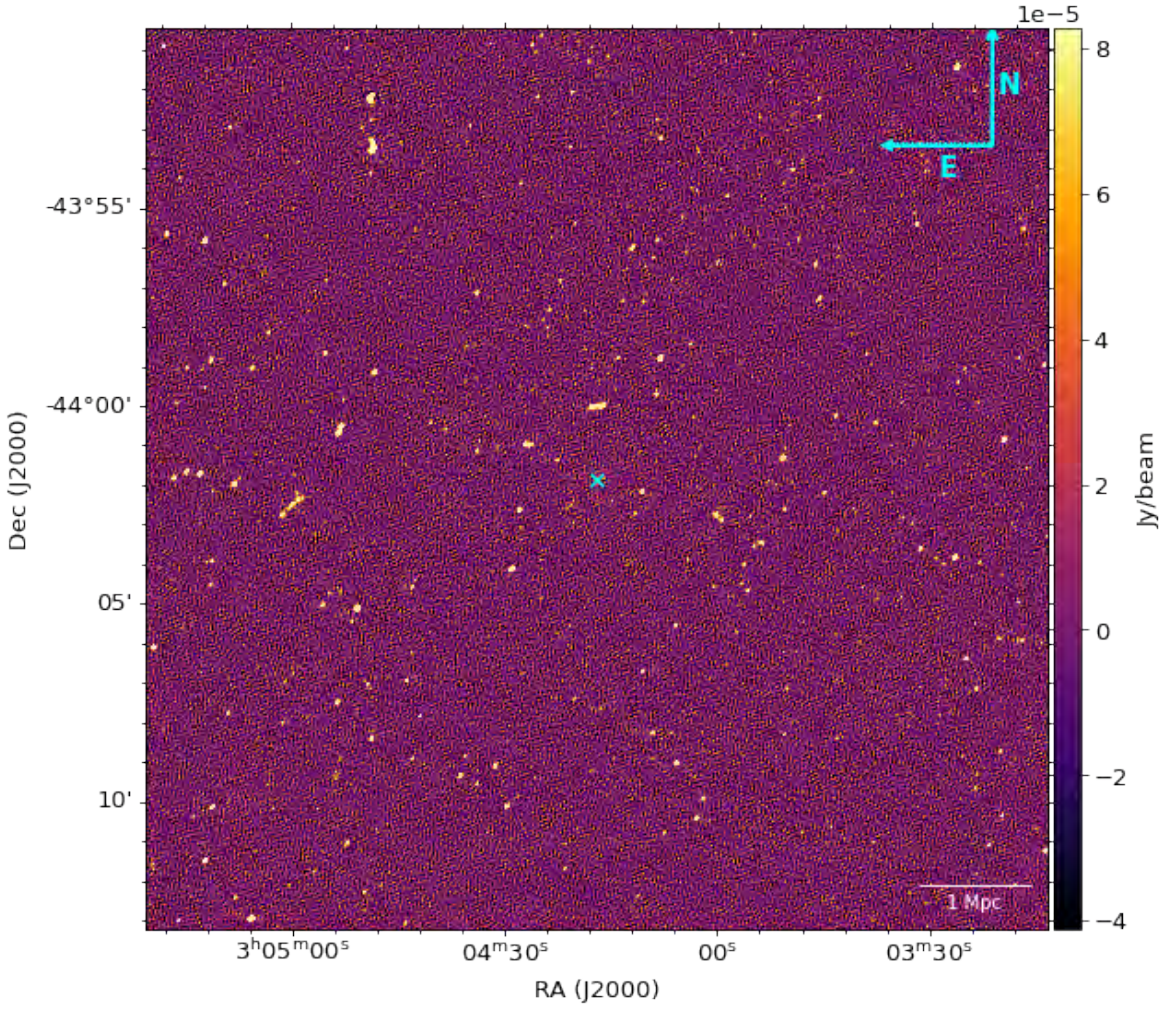

Figure 2.6: Uniform-weighted image of the PSZ2G254 field at 1.28 GHz. The image has a 20 μJy beam^{-1} rms noise and a $4.72'' \times 3.59''$ angular resolution.

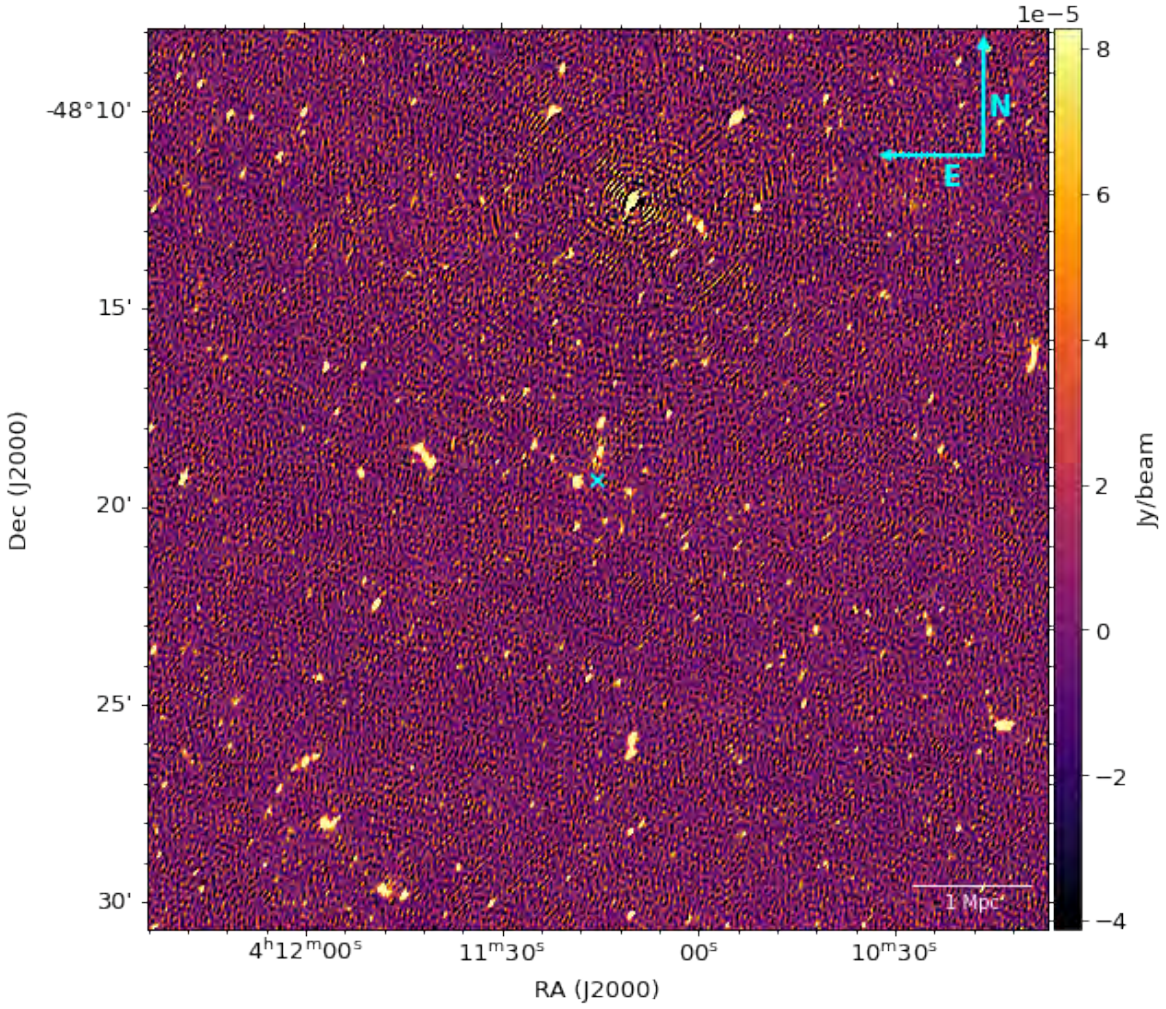

Figure 2.7: Uniform-weighted image of the PSZ2G255 field at 1.28 GHz. The image has a 22.5 μJy beam^{-1} rms noise and a $7.54'' \times 3.96''$ angular resolution.

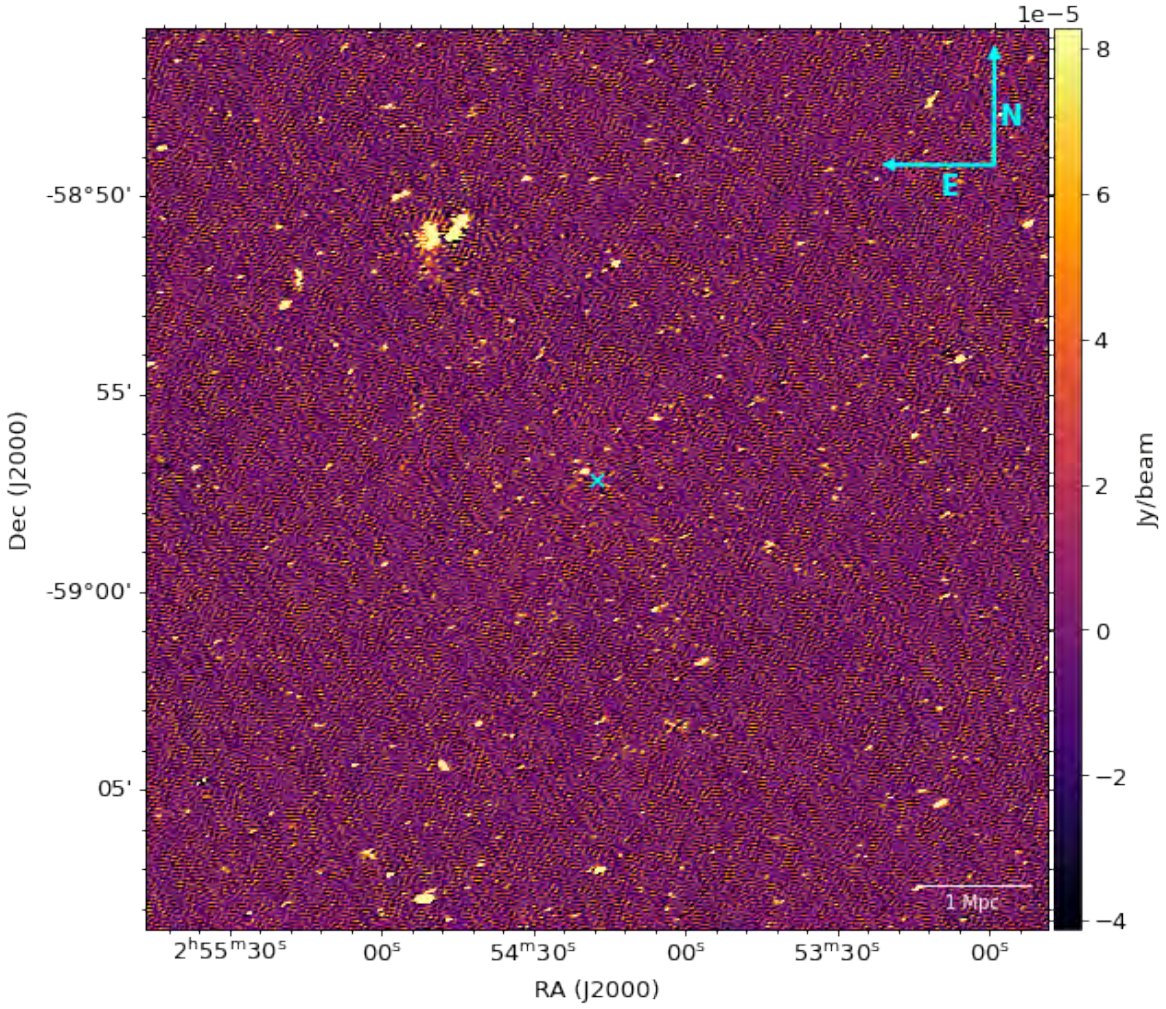

Figure 2.8: Uniform-weighted image of the PSZ2G277 field at 1.28 GHz. The image has a 23.5 μJy beam^{-1} rms noise and a $6.46'' \times 3.06''$ angular resolution.

5. Repeat steps 1 and 2 while performing the `f-slope` calibration at finer solution intervals of 64 s, and halt the process until there is no apparent improvement in the images.

Final images after self-calibration are shown in Fig. 2.6, 2.7 and 2.8 for the three clusters, respectively. The images are centred in the respective clusters and indicated by the cyan cross. No particular artefact is visible in the self-calibrated images, apart from some residual errors surrounding a source located $\sim 7'$ from the centre of PSZ2G255 (Fig. 2.7) and residual sidelobes from a source outside the field of view of the PSZ2G277 cluster (Fig. 2.8). Although, the sidelobes in both images may improve with the implementation of 3GC. Neither of the sources appears, however, as a severe contamination at the cluster centre location. We can, therefore, conclude that our high-resolution images are noise limited and do not show any evidence of diffuse emission at the cluster location. In the next section, we will generate low-resolution images in order to increase the surface brightness sensitivity and search for diffuse emission at the cluster location.

CHAPTER 3

Radio Analysis and Results

In this chapter, we present the search for radio halos. All the images presented in this chapter have a FOV of $4.2' \times 4.2'$ with the cluster centre indicated with a green cross.

3.1 Diffuse Radio Emission in PSZ2G254.08-58.45

In order to increase the sensitivity to diffuse emission, we identified all the compact sources brighter than 0.4 mJy beam^{-1} in Fig. 2.6 and subtracted them from the visibilities using `uvsub` – a CASA task that subtracts the model visibility data from the corrected visibility data, which results in residuals, without touching the raw data column in the MS file. The subtracted sources were picked out in the $2.2^{\circ} \times 2.2^{\circ}$ FOV based on the post-2GC model image. As the model image shows sources recorded in the model visibility data, we were able to inspect whether true sources are detected and if a deeper mask (thresholds between $4-5$ times the source brightness) is required when imaging to model extended sources.

The residual image appears fairly featureless with no evidence of diffuse emission (Fig. 3.1). To increase the sensitivity to diffuse emission, we chose a Briggs weighting with `robust=0`

Table 3.1: Image properties and parameters of the cluster sample: (1) cluster name; (2) angular resolution; (3) noise rms; (4) Gaussian taper used.

Cluster Name	Resolution ($''\times''$)	$\sigma_{\rm rms}$ (μJy beam^{-1})	Gaussian taper ($''$)
PSZ2G254.08-58.45	4.72 × 3.59	20	0
	8.00 × 6.01	5.8	0
	35.33 × 32.18	46.7	28
PSZ2G255.60-46.18	7.54 × 3.96	22.5	0
	10.85 × 6.92	11.3	0
	31.75 × 25.52	44.5	25
PSZ2G277.76-51.74	6.45 × 3.06	23.5	0
	11.84× 6.62	9.1	0
	35.98 × 24.67	32.7	20

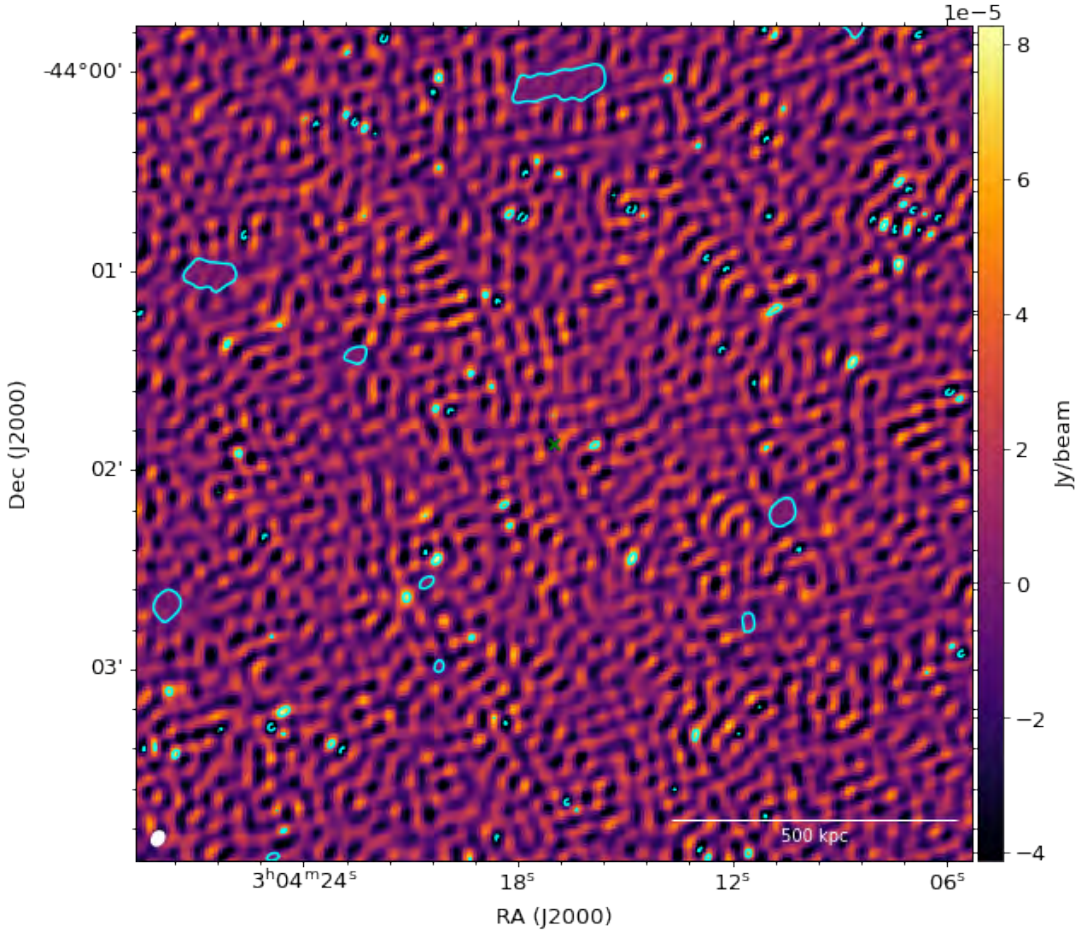

Figure 3.1: A zoom into the central part of the PSZ2G254 field (Fig. 2.6) after all the sources brighter than 0.4 mJy were subtracted. The image has a 20 μJy beam^{-1} rms noise and a $4.72'' \times 3.59''$ angular resolution. Cyan contours are drawn at 3σ level, and the white ellipse on the bottom-left corner is the synthesized beam size.

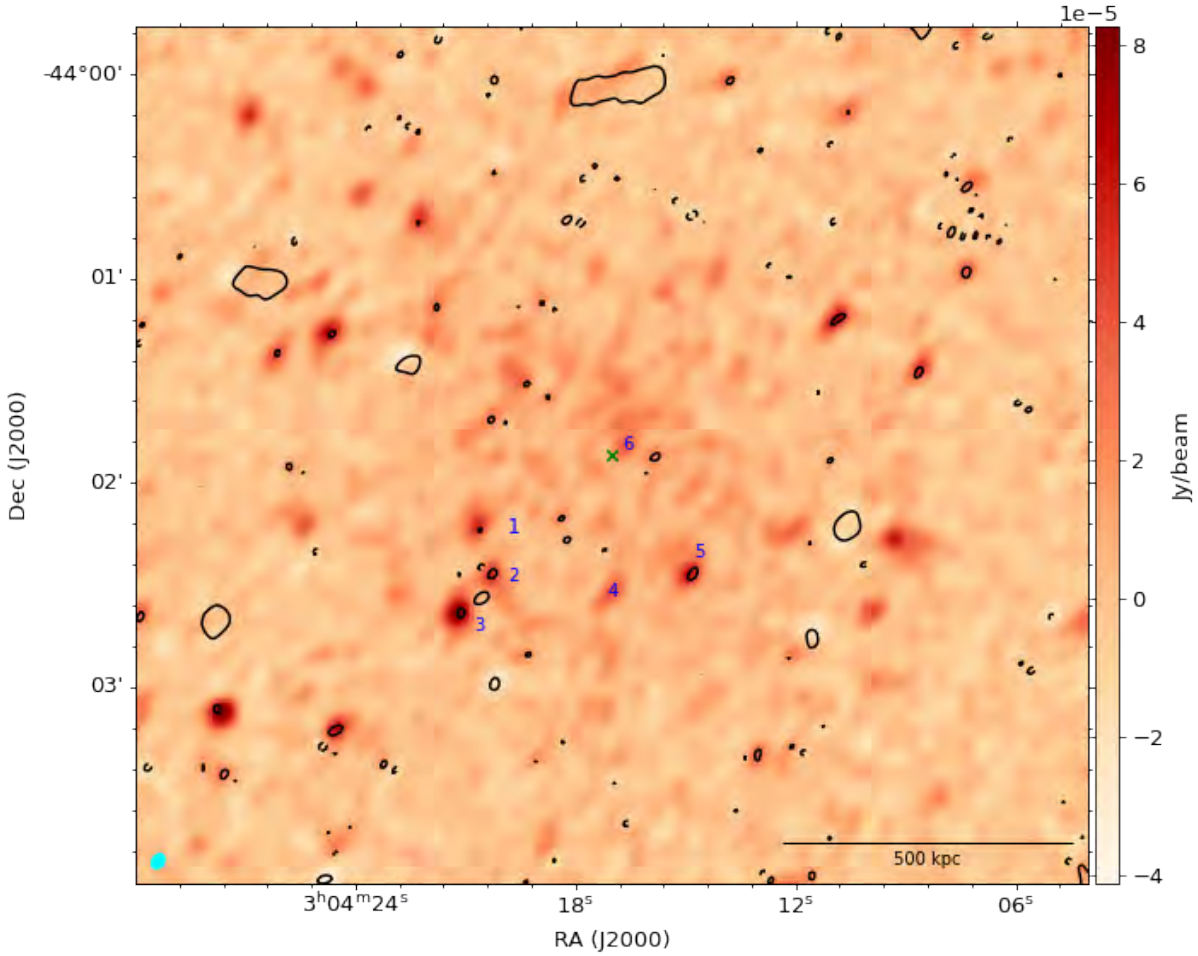

Figure 3.2: Same as Fig. 3.1, but with Briggs weighting `robust = 0`, yielding to a $8.00'' \times 6.01''$ angular resolution. Contours are drawn at -3σ (dashed line) and 3σ levels (solid line), where $\sigma = 5.8$ μJy beam^{-1}. The numbers $1 - 6$ indicate residual sources that are visible at a lower resolution. The cyan ellipse on the bottom-left corner indicates the beam.

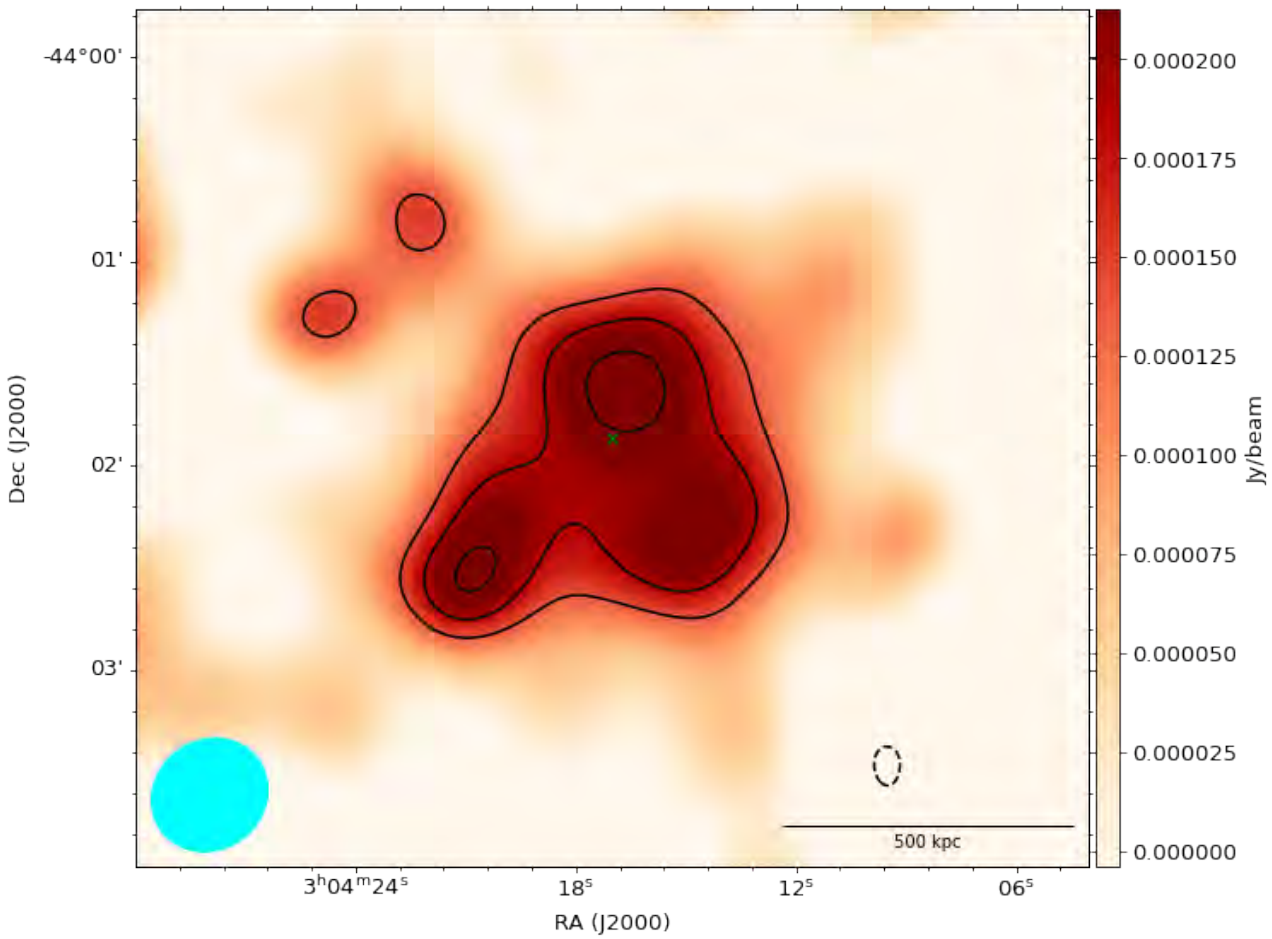

Figure 3.3: Low resolution image of PSZ2G254 at 1.28 GHz after subtracting sources $1-6$ in Fig. 3.2. The image is a result of Briggs weighting with `robust = 0.5` and a Gaussian taper of 28″, yielding a resolution of $35.3'' \times 32.2''$. Contours are drawn at [-3, 3, 4, 5] $\times\sigma$ levels, where $\sigma = 46.7$ μJy beam^{-1} showing extended diffuse emission at the centre. The cyan ellipse on the bottom left corner indicates the beam.

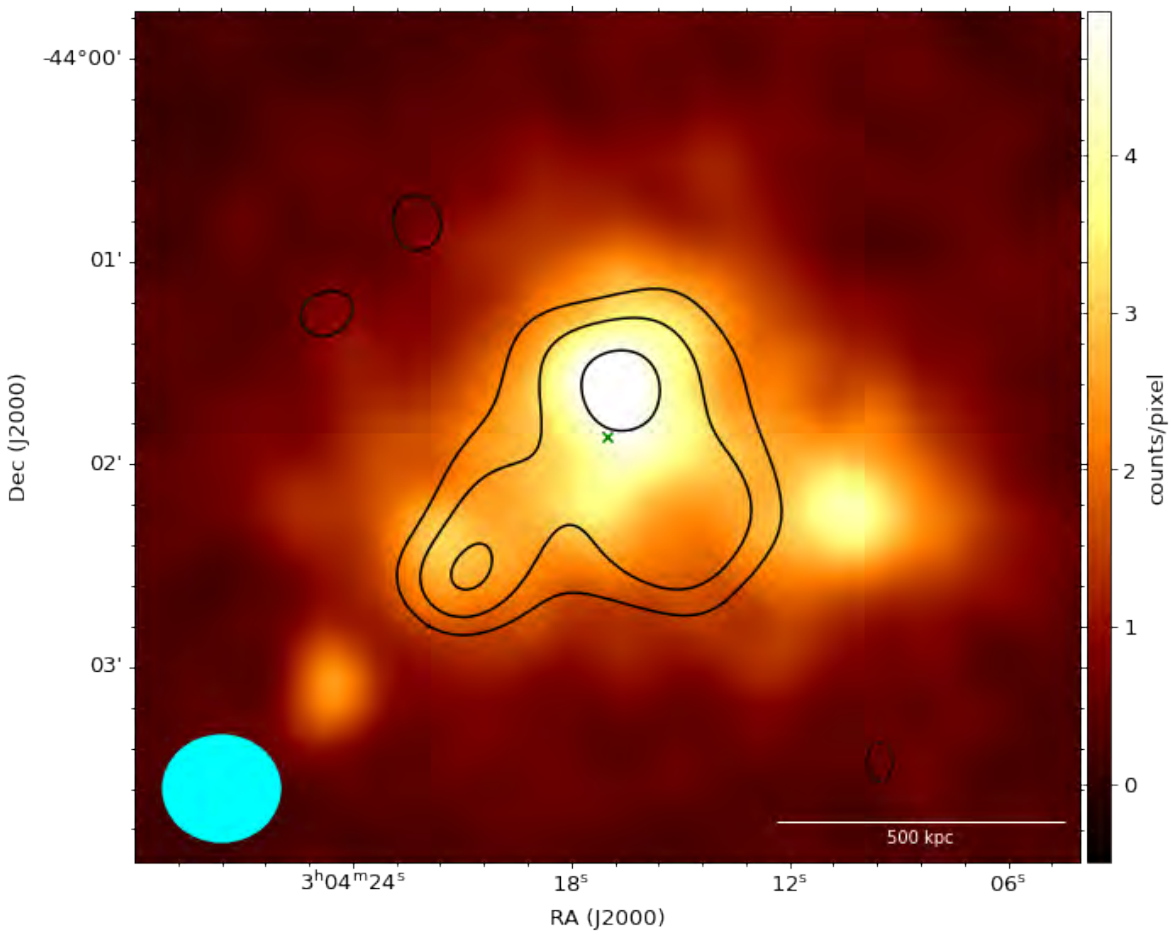

Figure 3.4: Low-resolution radio contours (Fig. 3.3) overlaid on the XMM-Newton image of PSZ2G254. The image highlights the morphological correspondence between radio and X-ray emission. The X-ray image is in the 1.0-8.0 keV band, which we smoothed with a 10-pixel Gaussian kernel. The cyan ellipse on the bottom left corner indicates the beam.

to generate an image with $8.00'' \times 6.01''$ angular resolution (Fig. 3.2). No particular evidence of diffuse emission is visible at such resolution either, although a few sources located in the area where a radio halo is expected appear now visible and are numbered $1 - 6$ in Fig. 3.2. From the high-resolution contours in Fig. 3.2, some of these sources are detected at 3σ but were not subtracted. This is likely due to the extended nature of the sources, such that they are not accurately modelled, and what we detect in the low-resolution image are the residuals. We further subtracted these sources using CRYSTALBALL[1] – a package that can predict the spectral shape of sources in a given region file and WSCLEAN source list into the model visibility data. We then generated a residual image with Briggs `robust=0.5` weight and a Gaussian taper of $28''$ to produce a low-resolution, $35.33'' \times 32.18''$ image (Fig. 3.3).

In Fig 3.3, diffuse emission is now clearly visible at the cluster centre location, with an approximate round morphology, extending over ~ 2 arcmin (at the 3σ contour), corresponding to a physical length of ~ 500 kpc. The brightness distribution peaks at ~ 250 μJy beam^{-1} and follows the X-ray morphology (Fig. 3.4), which leads us to classify the extended emission as a radio halo.

We computed the flux density $S_{1.28\,\mathrm{GHz}}$ using the CASA task `imstat` and the uncertainty on the flux density as (Cassano et al., 2013; Kale et al., 2015):

$$\Delta S_\nu = \sqrt{(\sigma_{rms}\sqrt{N_{beam}})^2 + (\sigma_{cal} S_\nu)^2}, \tag{3.1}$$

where σ_{rms} is the map rms noise, N_{beam} is the number of independent beams in the region of the halo and σ_{cal} is the calibration uncertainty. To determine σ_{cal}, we applied the CARACAL gain and bandpass solutions from the PSZ2G254 calibration onto the 3C286 observations included in our data. We created image cubes of 3C286 using WSCLEAN and measured the flux density at the respective central frequencies. The comparison between the obtained flux density vs frequency plot and the 3C286 model from Perley & Butler (2017) is shown in Fig. 3.5. We calculated a mean relative error percentage corresponding to the calibration error as $\sim 2\%$. Thus the operation resulted in a radio halo flux density at 1.28 GHz of 1.20 ± 0.08 mJy, integrated above the 3σ contour level.

[1] https://github.com/caracal-pipeline/crystalball.git

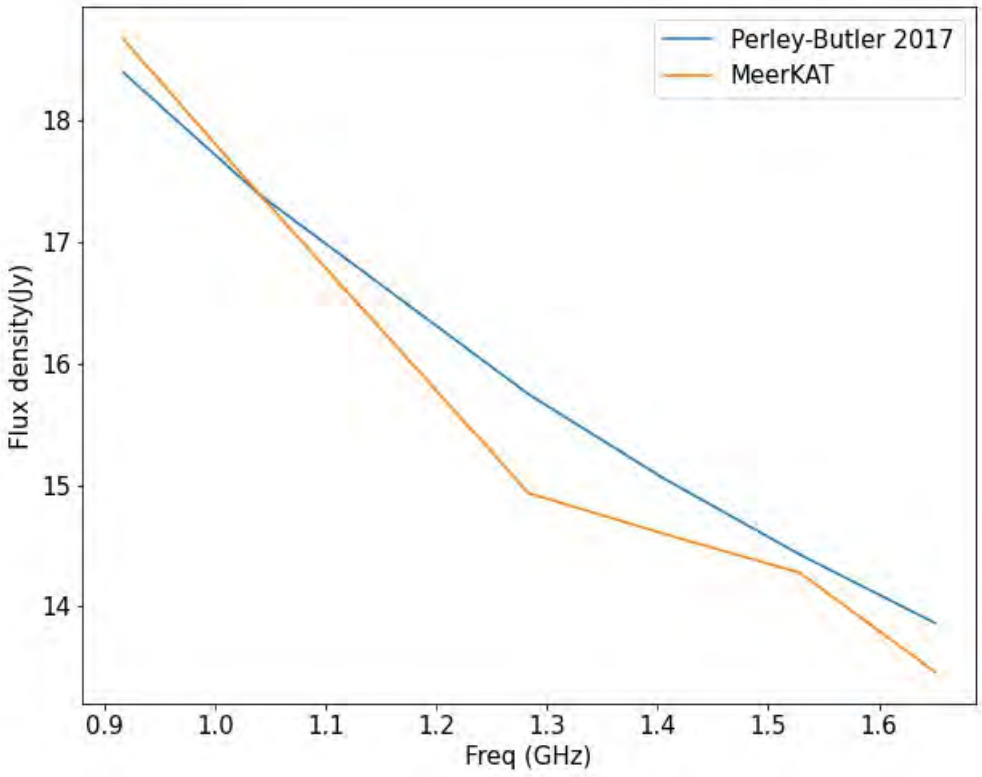

Figure 3.5: The flux comparison between the Perley & Butler (2017) model and calibrated MeerKAT observations of 3C286. The *blue* curve represents the Perley & Butler (2017) 3C286 model while the *orange* one shows 3C286 as observed by MeerKAT.

3.2 The PSZ2G255.60-46.18 Field

We repeated the same steps and identified the sources the same way as PSZ2G254. No evidence of diffuse emission appears in the high-resolution images of this field after all the sources brighter than 0.1 mJy were subtracted (Fig. 3.6). In order to increase the sensitivity to diffuse emission, we follow the same procedure of Sec. 3.1 and imaged the residual visibilities at Briggs weighting with `robust=0` and generated a $10.9'' \times 6.9''$ resolution image (Fig. 3.7). Even at this resolution, no diffuse emission is detectable, although seven sources are now visible in the central region of the field, numbered $1 - 7$. We further modelled and subtracted them from the visibilities and imaged the residuals at Briggs weighting with `robust = 0.5` and a Gaussian taper of $25''$. The resulting image has a resolution of $31.8'' \times 25.5''$ and also shows no hint of extended emission at the centre (Fig. 3.8).

As a result of this non-detection, we placed upper limits on the flux density of a radio halo. We adopted the method of injecting mock radio halos in the visibilities, following previous studies of upper limits determination (Venturi et al., 2007; Kale et al., 2013, 2015; Cuciti et al., 2018, 2021a). We used the ULCALC[2] software package, which allows generating various types of radio halo models (George et al., 2021). Following Cuciti et al. (2021a), the radio halo brightness profile was modelled using the exponential profile in Eq. 1.13. The redshift, cluster name and position to inject the mock halo were required as inputs in the PSZ2G255 field.

The model generated was then Fourier transformed into visibilities and added to the source-subtracted visibilities (i.e. the one used to generate the lowest resolution image, Fig. 3.8). These "injected" visibilities were then imaged again using the same imaging parameters as Fig. 3.8. We expect that faint halos would still be undetected in our images where there is a flux density value for which the injected halo is detected with statistical significance. In order to determine the statistical significance of the upper limit, we assume that the radio halo would have a similar extent to what was observed in the PSZ2G254 cluster, i.e. $\sim 2'$, given that they have a similar redshift. We, therefore, obtained the flux density $F_{\rm res}$ by integrating over a circular area of $1'$ radius of our residual image (Fig. 3.8), centred on the cluster centre. Similarly, we computed the

[2]https://github.com/lijotgeorge/UL-CALC.git

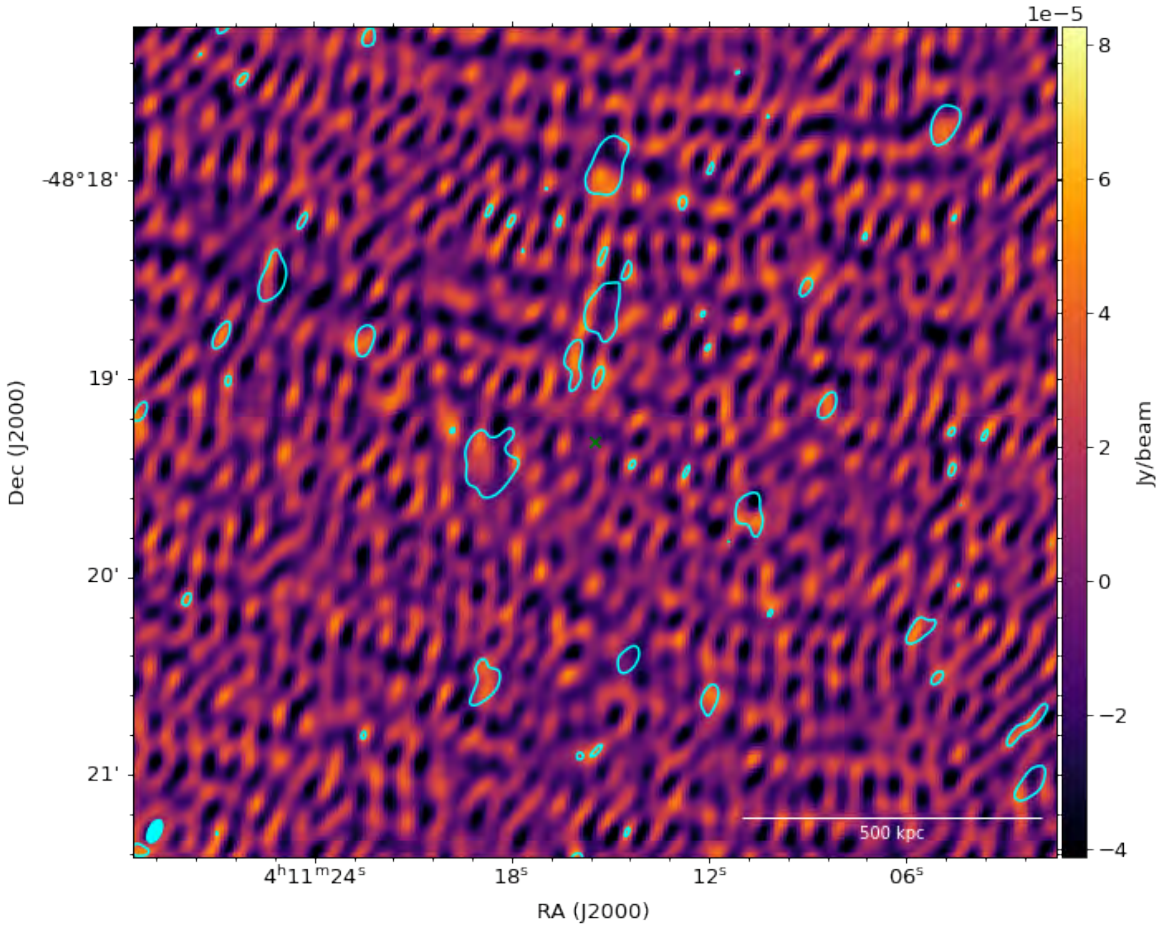

Figure 3.6: A zoom into the central part of the PSZ2G255 field (Fig. 2.7) after all the sources brighter than 0.1 mJy were subtracted. The image has a 22.5 μJy beam^{-1} rms noise and a 7.5″ $\times$ 4.0″ angular resolution. Cyan contours are drawn at 3σ level, and the cyan ellipse on the bottom-left corner is the synthesized beam size.

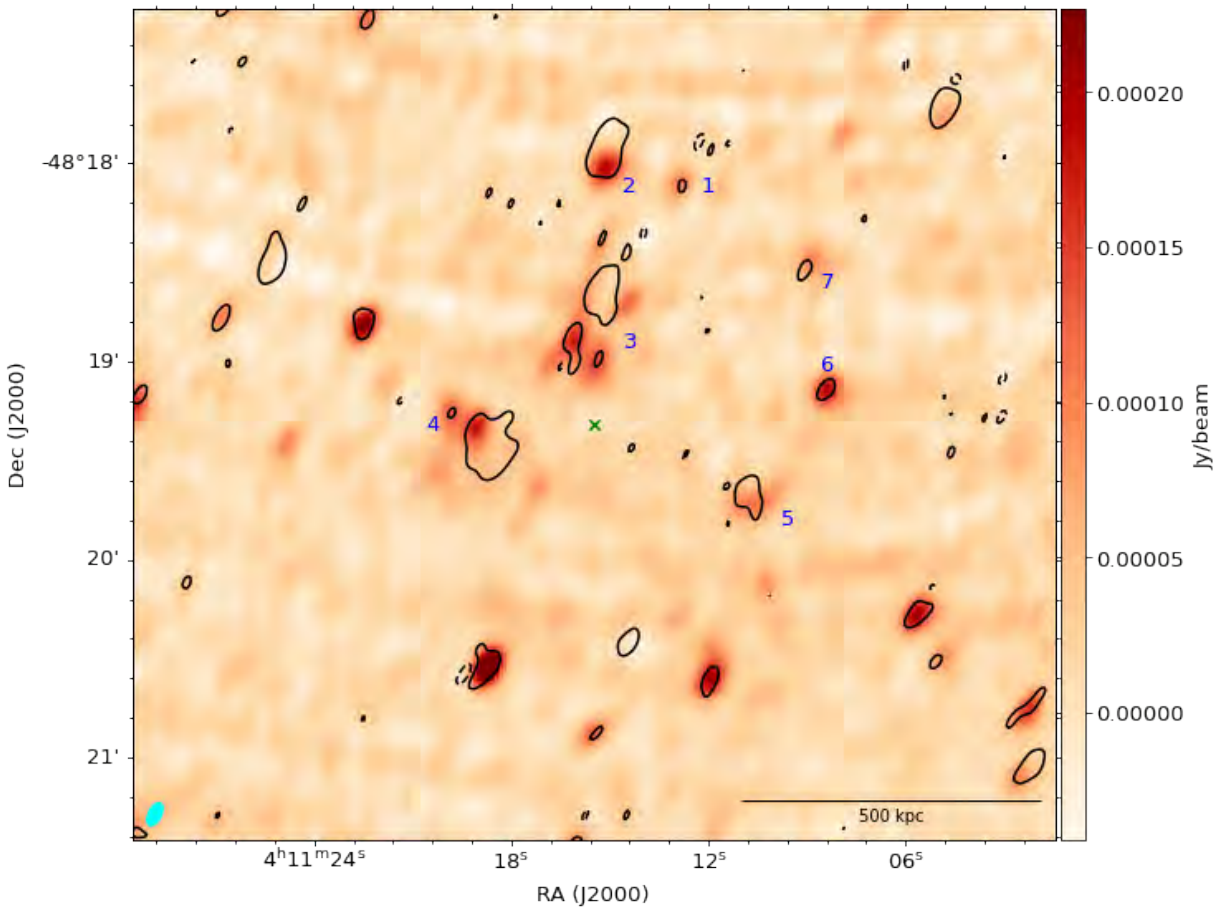

Figure 3.7: Same as Fig. 3.6, but with Briggs weighting `robust = 0`, yielding to a $10.9'' \times 6.9''$ angular resolution. Contours are drawn at -3σ (dashed line) and 3σ levels (solid line), where $\sigma = 11.3$ μJy beam^{-1}. The numbers $1 - 7$ indicate residual sources that are visible at a lower resolution. The cyan ellipse on the bottom-left corner indicates the beam.

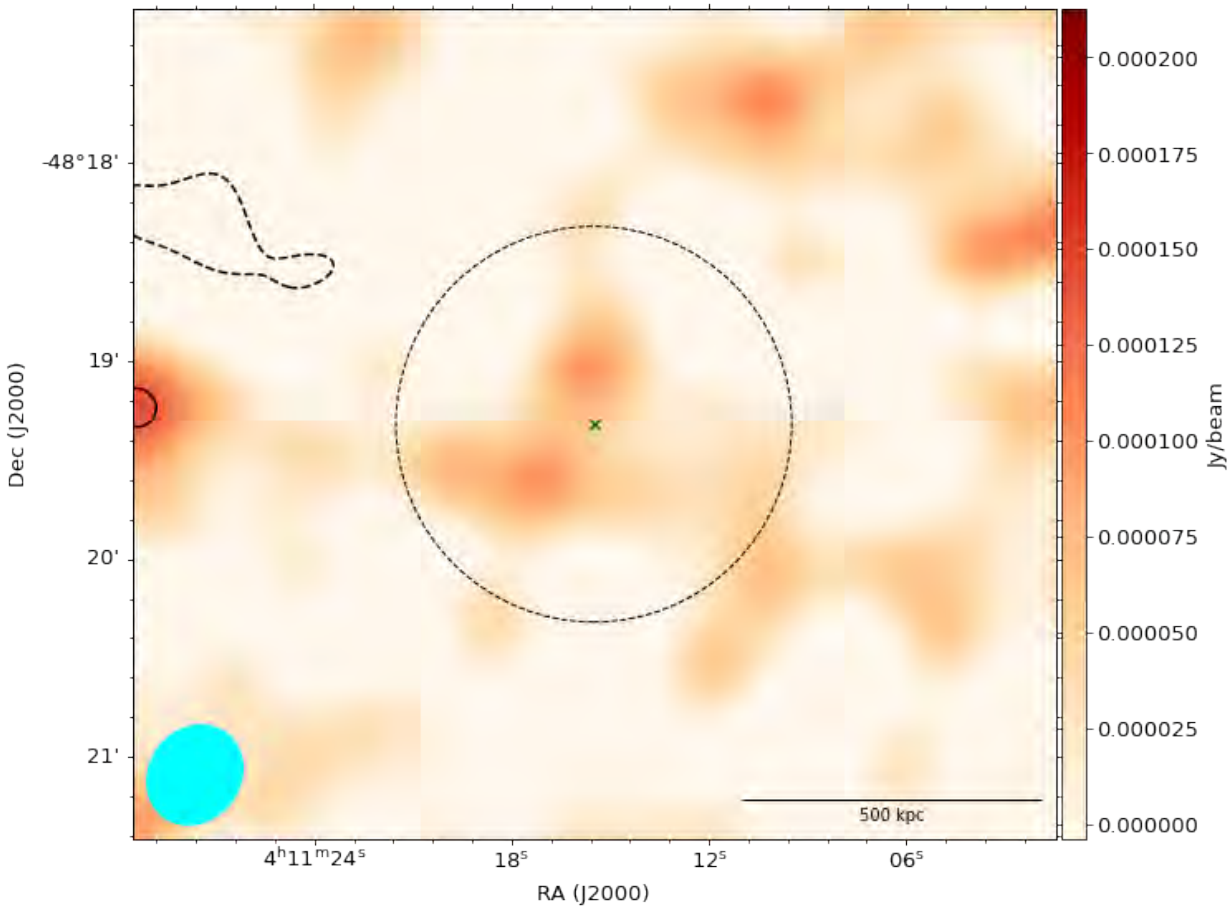

Figure 3.8: Low resolution image of the PSZ2G255 field at 1.28 GHz, after subtracting sources $1-7$ in Fig. 3.7. The image is a result of Briggs weighting with `robust = 0.5` and using a Gaussian taper of $25''$, yielding image has a resolution of $31.8'' \times 25.5''$. Contours are drawn at [-3, 3]$\times\sigma$ levels, where $\sigma = 44.5$ μJy beam^{-1}, showing no hint of central diffuse emission. The cyan ellipse on the bottom left corner indicates the beam, and the dashed circle shows the $1'$ integrating region.

flux density $F_{\rm inj}$ over the same area after injecting a radio halo model. Image examples where model radio halos were injected into visibilities are shown in Fig. 3.9. The injected radio halo is more visible as the flux density increases.

Following Nunhokee et al. (2017), we defined a ratio R:

$$R(F_{\rm inj}) = \frac{F_{\rm inj} - F_{\rm res}}{F_{\rm res}}, \tag{3.2}$$

computed for halos whose injected flux density spanned the $[0.0 - 1.0]$ mJy range, in steps of 0.02 mJy.

We then constructed the cumulative distribution function $P(R)$, from which we calculated 0.99 mJy corresponding to $P(R) = 0.95$ (Fig. 3.10). This sets the 95% upper limit to the halo flux density in our observations.

3.3 The PSZ2G277.76-51.74 Field

We followed the same procedure as in the previous targets and identified sources brighter than 1.2 mJy. The sources are relatively brighter as some faint sources were masked to avoid including artefacts visible in deeper masks. We found that even in the case of this cluster target, the high-resolution image reveals no evidence of diffuse emission at the cluster centre (Fig. 3.11).

In order to increase surface brightness sensitivity, we imaged the source-subtracted visibilities at Briggs weighting with `robust = 0` to produce an image with $11.8'' \times 6.6''$ angular resolution (Fig. 3.12). This image reveals sources embedded in the centre, which we numbered $1-6$, but showed no hint of diffuse emission. We subtracted the source and imaged the residuals using Briggs weighting with `robust = 0.5` and a Gaussian taper of $20''$. The final image has an angular resolution of $36.0'' \times 24.7''$ but still shows no evidence of diffuse emission (Fig. 3.13).

We determined an upper limit to the radio halo flux density following the same procedure as in PSZ2G255. Examples of images where the flux density radio halo was injected in the visibilities are shown in Fig. 3.14. By constructing the cumulative distribution function, we determined a 95% upper limit on the radio halo flux density of 0.96 mJy (Fig. 3.10).

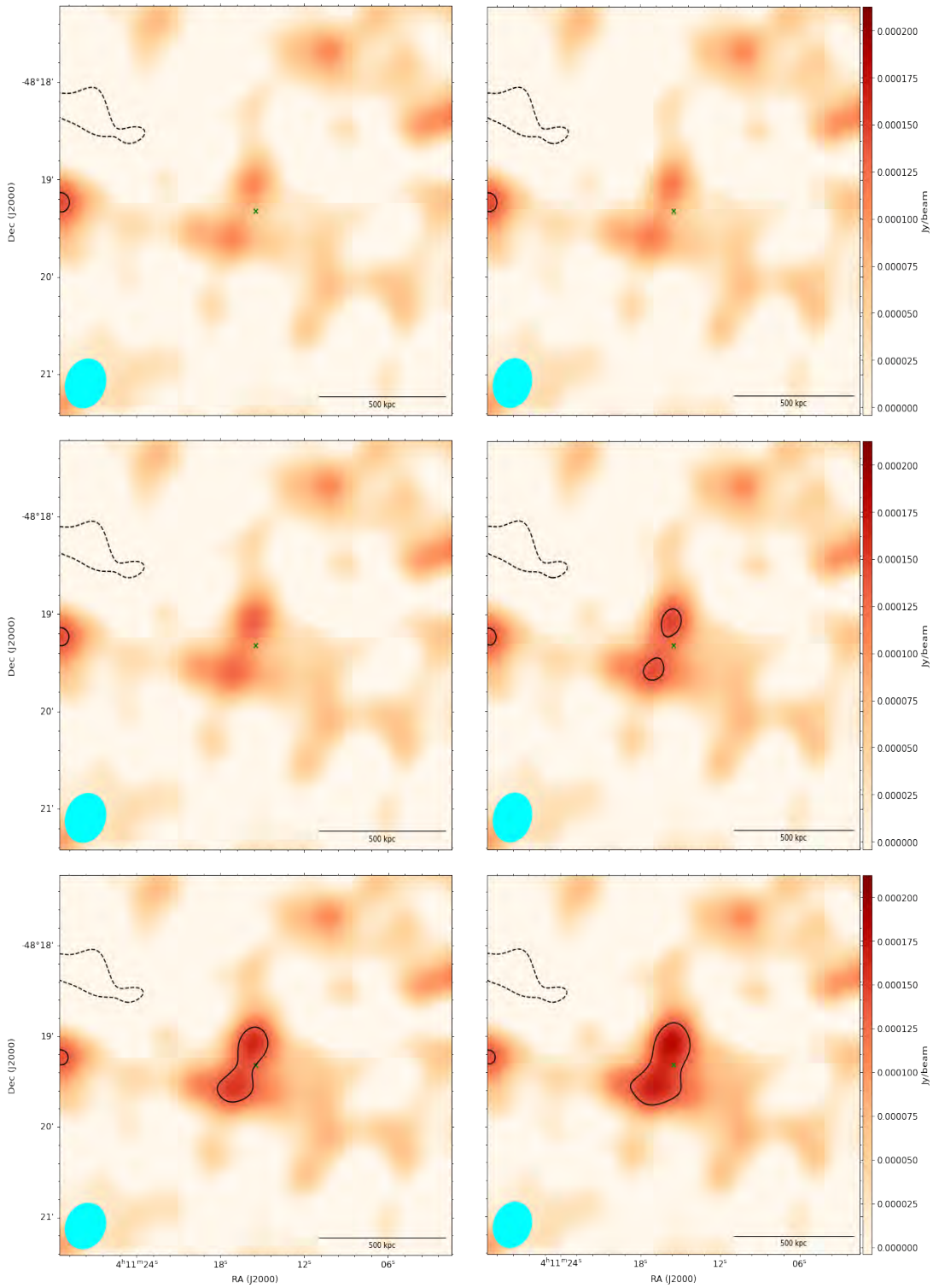

Figure 3.9: Image examples of mock halos injected in the PSZ2G255 observations. The overlaid dashed and solid contours are at -3σ and 3σ, respectively, where $\sigma = 44.5$ μJy beam^{-1}. Injected flux densities run from 0.1 (top left), 0.2 (top right), 0.4 (middle left), 0.6 (middle right), 0.8 (bottom left) and 1 mJy (bottom right). The injected halo is clearly visible with respect to the observed image (Fig. 3.8) as its flux density increases. The beam size is shown as a cyan ellipse at the bottom-left corner of each sub-image.

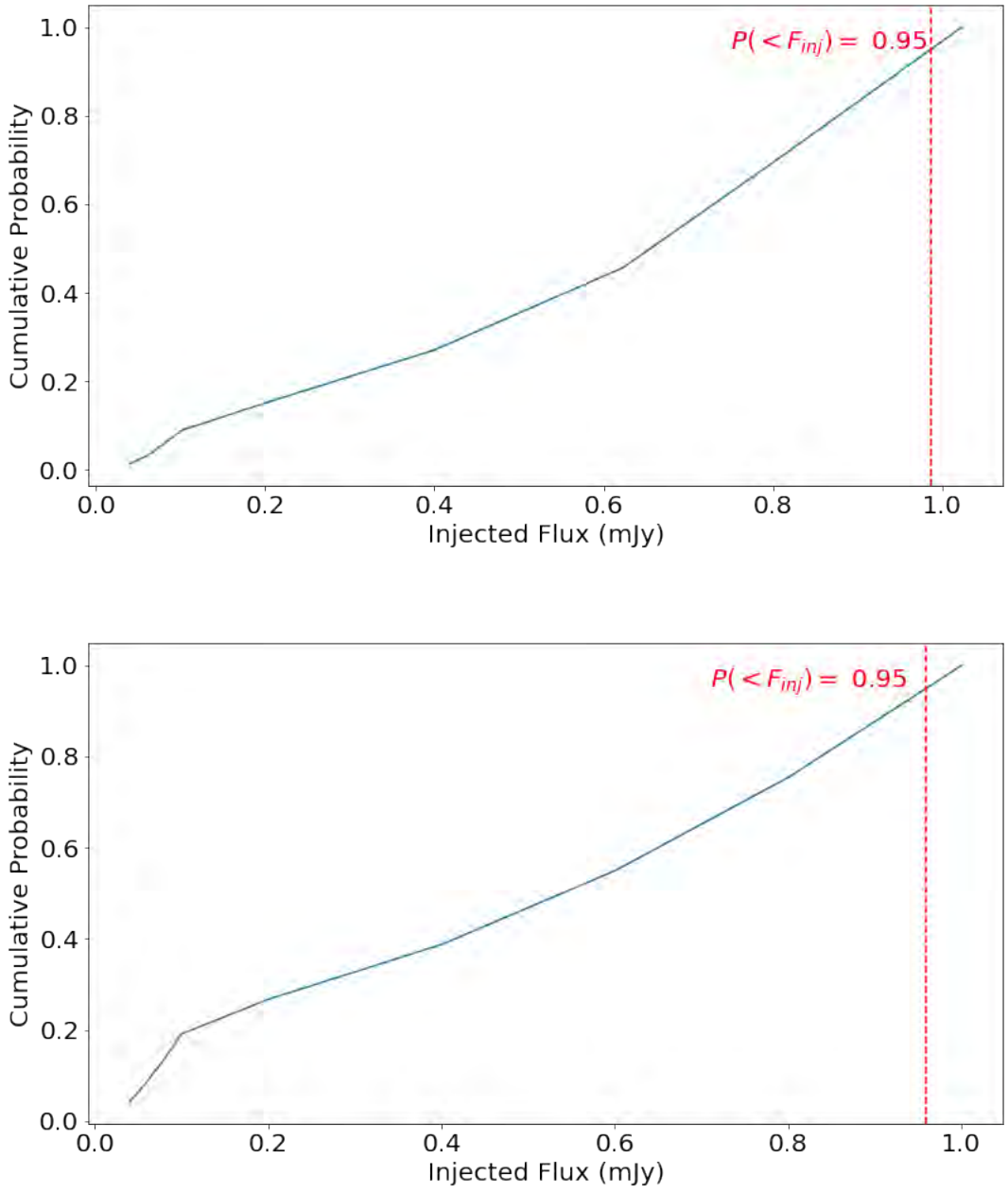

Figure 3.10: Cumulative distribution plot of the mock halo injection for the cluster PSZ2G255 (top) and PSZ2G277 (bottom) in blue. The red dotted line indicates the flux density value corresponding to $P(< R) = 0.95$.

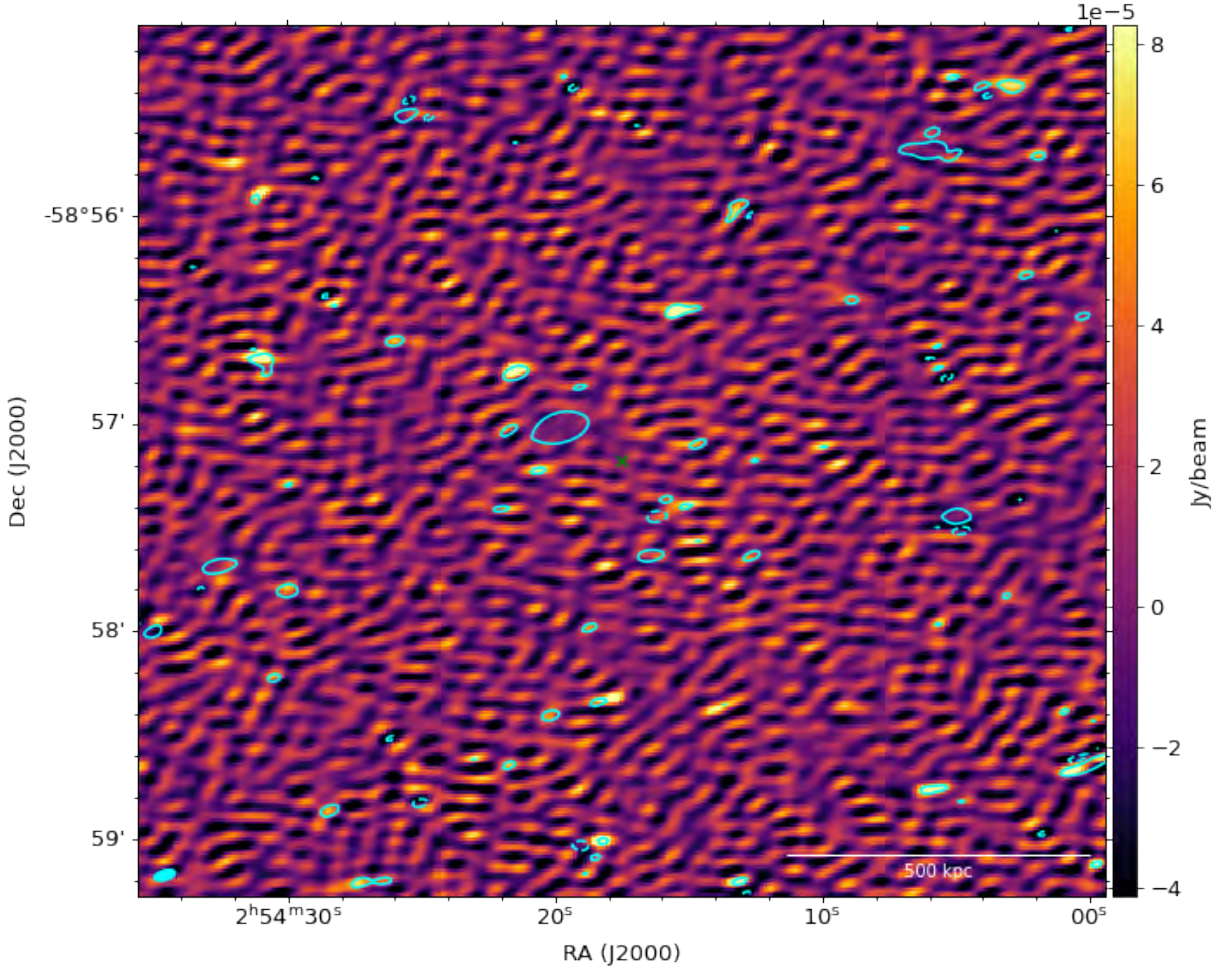

Figure 3.11: A zoom into the central part of the PSZ2G277 field (Fig. 2.8) after all the sources brighter than 1.2 mJy were subtracted. The image has a 23.5 μJy beam^{-1} rms noise and a $6.5'' \times 3.1''$ angular resolution. Cyan contours are drawn at 3σ level, and the cyan ellipse on the bottom-left corner is the synthesized beam size.

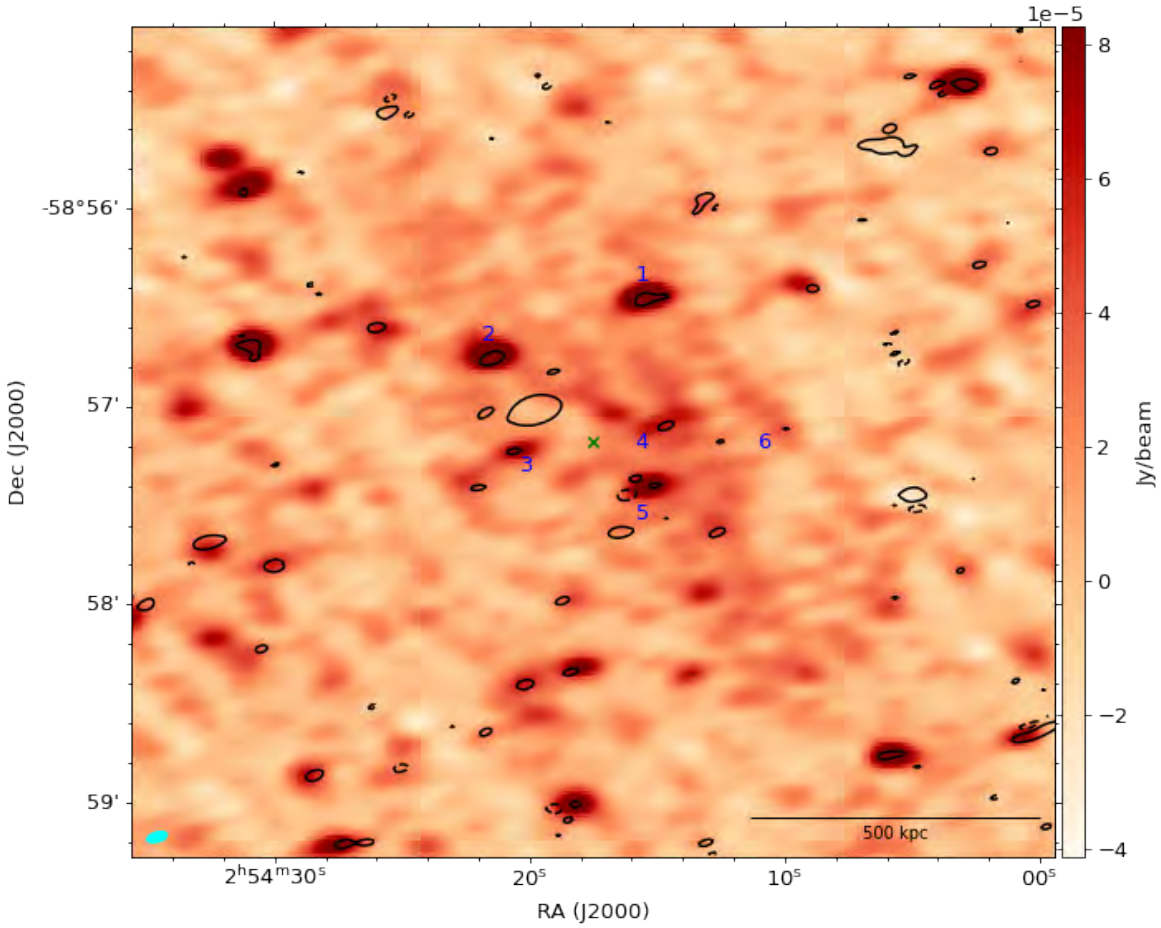

Figure 3.12: Same as Fig. 3.11, but with Briggs weighting `robust = 0`, yielding to a $11.84'' \times 6.62''$ angular resolution. Contours are drawn at -3σ (dashed line) and 3σ levels (solid line), where $\sigma = 9.1\ + \mu$Jy beam^{-1}. The numbers $1 - 6$ indicate residual sources that are visible at a lower resolution. The cyan ellipse on the bottom-left corner indicates the beam.

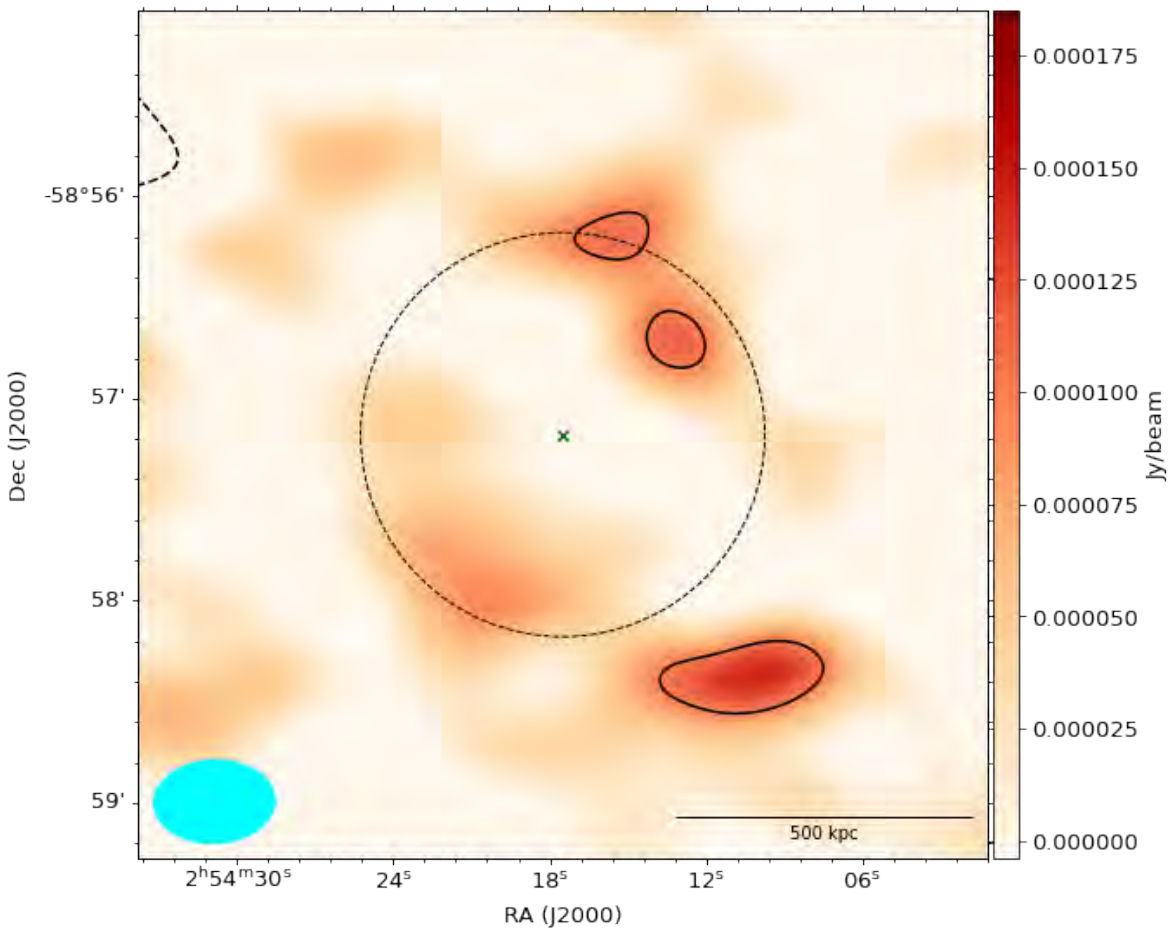

Figure 3.13: Low resolution image of PSZ2G277 at 1.28 GHz after subtracting sources $1-6$ in Fig. 3.12. The image is a result of Briggs weighting with `robust = 0.5` and using a Gaussian taper of 20″, yielding image has a resolution of 35.97″×24.67″. Contours are drawn at [-3, 3]×σ levels, where $\sigma = 32.7\ + \mu$Jy beam^{-1} showing no hint of central diffuse emission. The cyan ellipse on the bottom left corner indicates the beam, and the dashed circle shows the $1'$ integrating region.

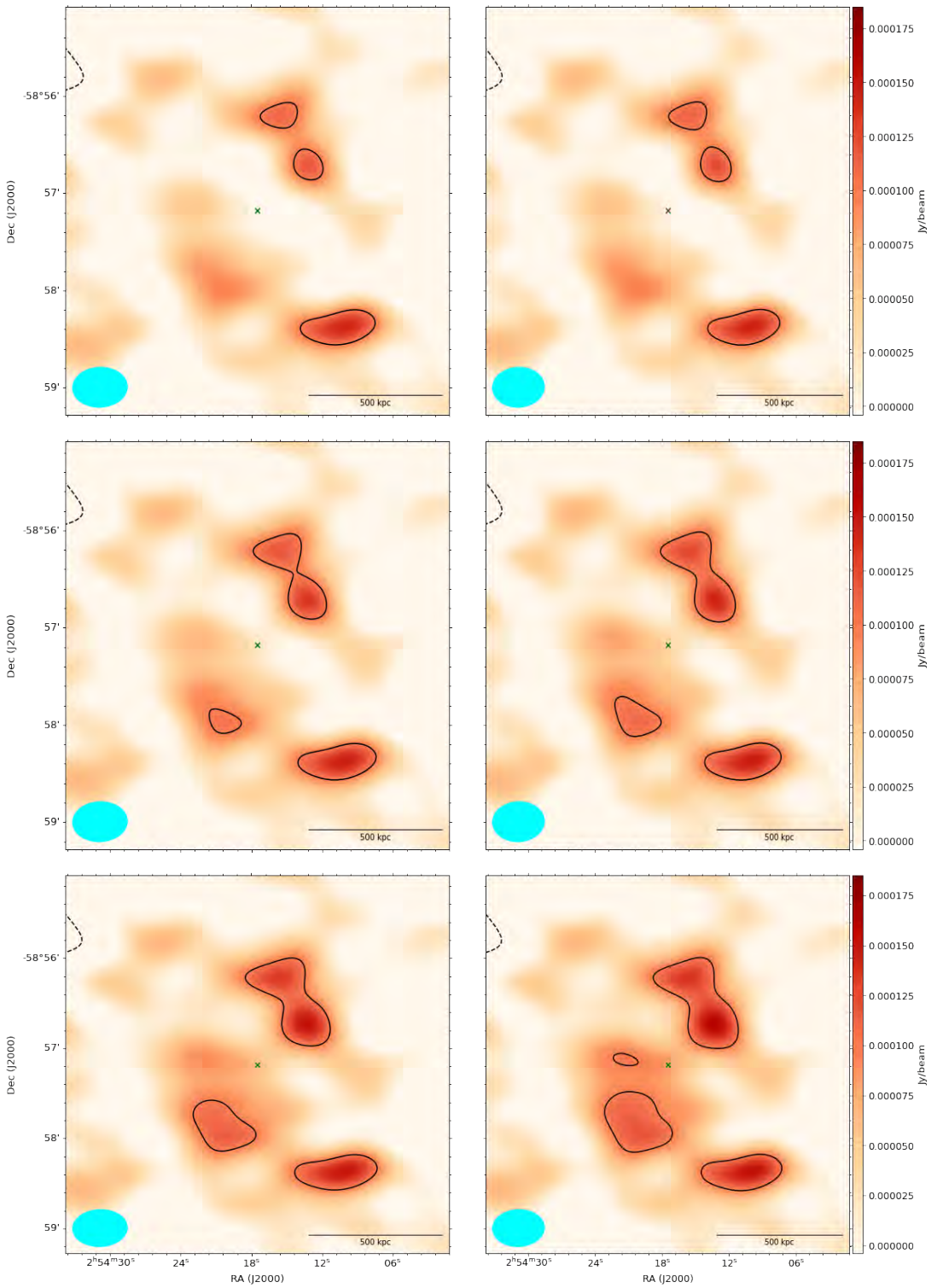

Figure 3.14: Image examples of mock halos injected in the PSZ2G277 observations. The overlaid dashed and solid contours are at -3σ and 3σ, respectively, where $\sigma = 32.7$ μJy beam^{-1}. Injected flux densities run from 0.1 (top left), 0.2 (top right), 0.4 (middle left), 0.6 (middle right), 0.8 (bottom left) and 1 mJy (bottom right). The injected halo is clearly visible with respect to the observed image (Fig. 3.13) as its flux density increases. The beam size is shown as a cyan ellipse at the bottom-left corner of each sub-image.

CHAPTER 4

Summary

In this chapter, we discuss our results and compare them with results in literature. We also provide our conclusions.

4.1 Discussion and Conclusions

We computed k-corrected radio powers $P_{1.4\ \mathrm{GHz}}$ for our detected radio halo and the derived upper limits as:

$$P_{1.4\ \mathrm{GHz}} = \frac{4\pi D_L^2}{(1+z)^{1+\alpha}} S_{1.4\ \mathrm{GHz}}, \tag{4.1}$$

where D_L is the luminosity distance and $S_{1.4\ \mathrm{GHz}}$ is the flux density at 1.4 GHz. We assumed a fiducial spectra index of $\alpha = -1.3$ (Table 4.1; Feretti et al., 2012; Cuciti et al., 2021a).

We included our results in the $P_{1.4\ \mathrm{GHz}} - M_{500}$ plot of the most recent large radio halo survey, even if it includes only candidates at $z < 0.4$ (Fig. 4.1; Cuciti et al., 2021b). The radio halo detected in PSZ2G254 is consistent with the radio power-mass correlation, and the upper limit on PSZ2G255 is not inconsistent with the correlation. Conversely, the upper limit on the PSZ2G277 case places any potential radio halo well below the correlation, with a five times improvement

over previous upper limits (Martinez Aviles et al., 2018). This may well be a peculiar case as its upper limit is approximately located in the area of ultra-steep spectrum radio halos (Cassano et al., 2013) that are, however, expected to be hosted by less massive halos though, i.e. $M_{500} < 5 \times 10^{14}$ M$_{\odot}$.

Although our sample is fairly small and does not provide stringent tests of radio-halo formation models, it allows us a few considerations. First, the chance of detecting a radio halo in three clusters is very small at our frequencies, somewhat around a few percent (Cassano et al., 2006). However, we detected one radio halo whose occurrence, albeit not inconsistent with models, is higher ($\sim 33\%$) than expectations.

Giovannini et al. (2020) observed a sample of seven clusters in the same redshift range as our sample and at a similar frequency (1.5 GHz). They detected five radio halos, with powers ranging from 1.4×10^{24} W Hz^{-1} till 2.4×10^{25} W Hz^{-1}, therefore with an occurrence quite a bit higher than in our case and with halos typically more powerful than what we found. Their typical size is also larger than what we found in this work. It is worth noting that our observations are generally more sensitive than theirs, making our observations the deepest to date at GHz frequencies in our redshift range. Although,

Our occurrence rate, radio power and halo size are also smaller compared to the results from Di Gennaro et al. (2021a) at 140 MHz, although a higher occurrence is expected at those frequencies. In conclusion, our observations do not disfavour the current model of radio halo formation based on the turbulent re-acceleration scenario.

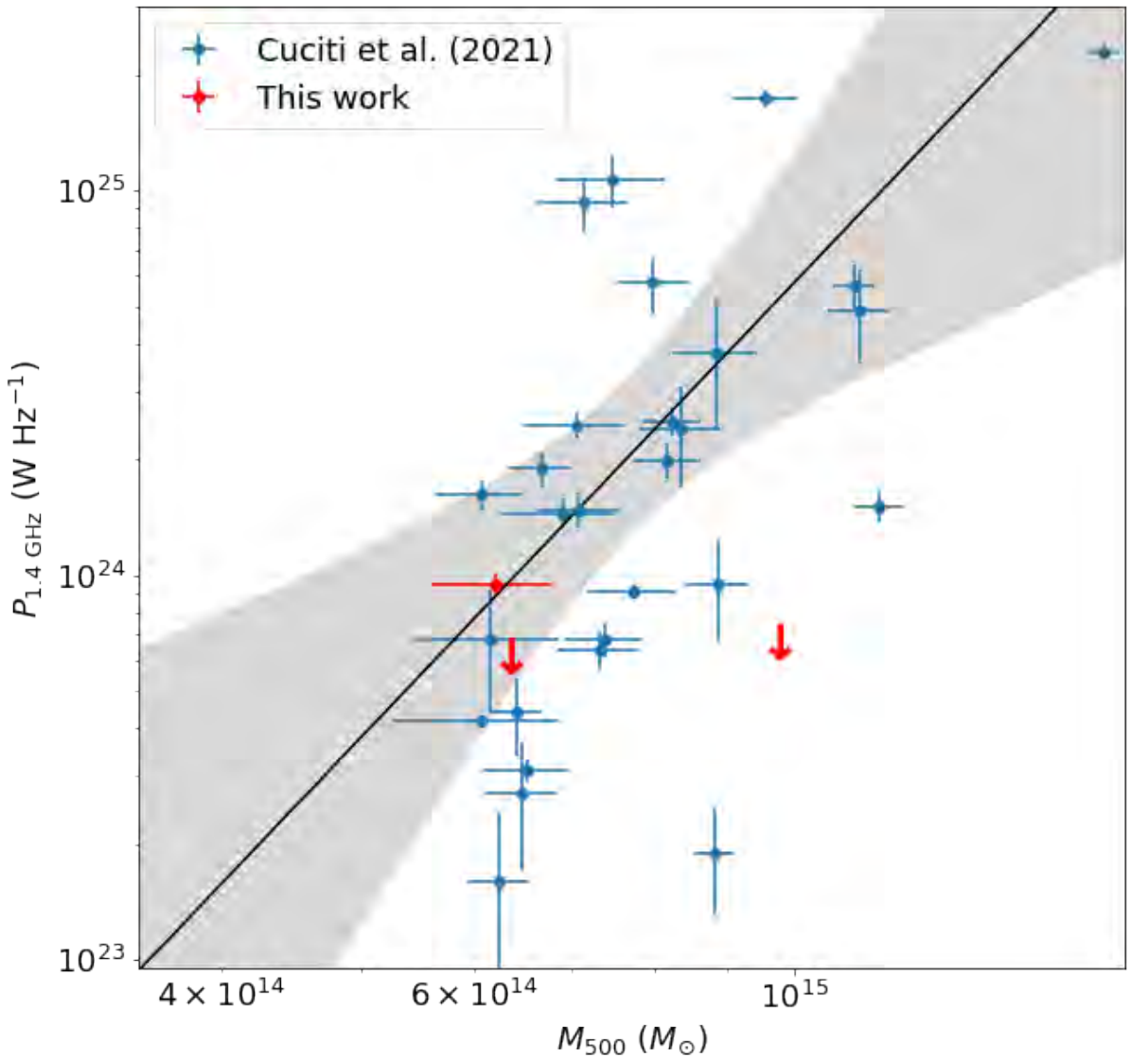

Figure 4.1: The $P_{1.4\ \mathrm{GHz}} - M_{500}$ plot for the radio sources in Table 4.1. The *blue* circles represent the radio halos detected by Cuciti et al. (2021a) while the *red* data points represent the radio halo detected (filled circle) and upper limits (arrows). The upper limits correspond to the top of the arrow. Here, the best-fit line is based on the coefficients from Cuciti et al. (2021a) where the grey shaded region shows the 95% confidence interval.

Table 4.1: Radio properties of our cluster sample. Columns: (1) cluster name; (2) 1.28 GHz flux density; (3) luminosity distance; (4) k-corrected radio halo power at 1.4 GHz – or related upper limit.

Cluster Name	$S_{1.28\ \mathrm{GHz}}$ (mJy)	D_L (Mpc)	$P_{1.4\ \mathrm{GHz}}$ (10^{23} W Hz^{-1})
PSZ2G254.08-58.45	1.20 ± 0.08	2563.9	9.43 ± 0.63
PSZ2G255.60-46.18	< 0.9	2301.1	< 6.22
PSZ2G277.76-51.74	< 0.96	2431.7	< 6.76

Bibliography

Abell, G. O. 1958, ApJS, 3, 211A

Allen, S. W., Evrard, A. E., & Mantz, A. B. 2011, AR&A, 49, 409

Arnaud, M., Pratt, G. W., Piffaretti, R., et al. 2010, A&A, 517, A92

Bagchi, J., Enßlin, T. A., Miniati, F., et al. 2002, New Astronomy, 7, 249

Bahcall, N. 1999a, ApJ, 525, 873

Bahcall, N. A. 1999b, Large-Scale Structure Formation: From the First Non-linear Objects to Massive Galaxy Clusters, ed. A. Dekel & J. P. Ostriker (Cambridge: Cambridge University Press), 135

Bartelmann, M. 2010, Classical and Quantum Gravity, 27, 233001

Bayliss, M. B., McDonald, M., Sharon, K., et al. 2020, Nature Astronomy, 4, 159

Bellagamba, F., Tessore, N., & Metcalf, R. B. 2016, MNRAS, 464, 4823

Bernardi, G., Venturi, T., Cassano, R., et al. 2016, A KAT-7 view of a low-mass sample of galaxy clusters, arXiv:1603.07595

Blasi, P., & Colafrancesco, S. 1999, Astrpart. Phys., 12, 169

Blasi, P., Gabici, S., & Brunetti, G. 2007, IJMPA, 22, 681

Bonafede, A., Feretti, L., Murgia, M., et al. 2010, A&A, 513, A30

Bonafede, A., Feretti, L., Giovannini, G., et al. 2009, A&A, 503, 707

Bonafede, A., Brüggen, M., van Weeren, R., et al. 2012, MNRAS, 426, 40

Bonafede, A., Cassano, R., Brüggen, M., et al. 2017, MNRAS, 470, 3465

Bonafede, A., Brunetti, G., Rudnick, L., et al. 2022, ApJ, 933, 218

Booth, R. S., de Blok, W. J. G., Jonas, J. L., & Fanaroff, B. 2009, MeerKAT Key Project Science, Specifications, and Proposals, arXiv:0910.2935

Booth, R. S., & Jonas, J. L. 2012, AfrSk, 16, 101

Botteon, A., Gastaldello, F., Brunetti, G., & Dallacasa, D. 2016a, MNRAS, 460, L84

Botteon, A., Gastaldello, F., Brunetti, G., & Kale, R. 2016b, MNRAS, 463, 1534

Botteon, A., Cassano, R., van Weeren, R. J., et al. 2021, ApJL, 914, L29

Botteon, A., Shimwell, T. W., Cassano, R., et al. 2022, A&A, 660, A78

Bower, R. G., Lucey, J. R., & Ellis, R. S. 1992, MNRAS, 254, 601

Briggs, D. S. 1995, PhD thesis, The New Mexico Institute of Mining and Technology

Brunetti, G., & Jones, T. W. 2014, Int. J. Mod. Phys. D, 23, 1430007

Brunetti, G., Setti, G., Feretti, L., & Giovannini, G. 2001, MNRAS, 320, 365

Brunetti, G., Zimmer, S., & Zandanel, F. 2017, MNRAS, 472, 1506

Brunetti, G., Giacintucci, S., Cassano, R., et al. 2008, Nature, 455, 944

Camilo, F., Scholz, P., Serylak, M., et al. 2018, ApJ, 856, 180

Carignan, C., Frank, B. S., Hess, K. M., et al. 2013, AJ, 146, 48

Carlstrom, J. E., Holder, G. P., & Reese, E. D. 2002, ARA&A, 40, 643

Cassano, R. 2010, A&A, 517, A10

Cassano, R., & Brunetti, G. 2005, MNRAS, 357, 1313

Cassano, R., Brunetti, G., & Setti, G. 2006, MNRAS, 369, 1577

Cassano, R., Brunetti, G., Setti, G., Govoni, F., & Dolag, K. 2007, MNRAS, 378, 1565

Cassano, R., Ettori, S., Brunetti, G., et al. 2013, ApJ, 777, 141

Cassano, R., Botteon, A., Gennaro, G. D., et al. 2019, ApJL, 881, L18

Chadayammuri, U., ZuHone, J., Nulsen, P., et al. 2021, MNRAS, 509, 1201

Clark, B. G. 1980, A&A, 89, 377

Condon, J. J., & Ransom, S. M. 2016, Essential Radio Astronomy (Princeton: Princeton University Press)

Cornwell, T., Golap, K., & Bhatnagar, S. 2008, IEEE Selected Topics in Sig. Proc., 2, 647

Cuciti, V., Brunetti, G., van Weeren, R., et al. 2018, A&A, 609, A61

Cuciti, V., Cassano, R., Brunetti, G., et al. 2015, A&A, 580, A97

—. 2021a, A&A, 647, A50

—. 2021b, A&A, 647, A51

de Gasperin, F., van Weeren, R. J., Brüggen, M., et al. 2014, MNRAS, 444, 3130

Dennison, B. 1980, ApJ, 239, L39

Di Gennaro, G., van Weeren, R. J., Brunetti, G., et al. 2021a, Nature Astronomy, 5, 268

Di Gennaro, G., van Weeren, R., Cassano, R., et al. 2021b, A&A, 654, A166

Diaferio, A., Schindler, S., & Dolag, K. 2008, Space Sci. Rev., 134, 7

Domínguez-Fernández, P., Vazza, F., Brüggen, M., & Brunetti, G. 2019, MNRAS, 486, 623

Donnert, J., Vazza, F., Brüggen, M., & J., Z. 2018, Space Sci. Rev., 214, 122

Enßlin, T. A., Biermann, P. L., Klein, U., & Kohle, S. 1998, A&A, 332, 395

Enßlin, T. A., & Gopal-Krishna. 2001, A&A, 366, 26

Enßlin, T. A., & Brüggen, M. 2002, MNRAS, 331, 1011

Ettori, S., Donnarumma, A., Pointecouteau, E., et al. 2013, Space Sci. Rev., 177, 119

Fabricant, D., Lecar, M., & Gorenstein, P. 1980, ApJ, 241, 552

Feretti, L., Giovannini, G., Govoni, F., & Murgia, M. 2012, A&AR, 20, 54

Forman, W., Jones, C., Cominsky, L., et al. 1978, ApJS, 38, 357

George, L., Kale, R., & Wadadekar, Y. 2021, Experimental Astronomy, 51, 235

Giovannini, G., Bonafede, A., Feretti, L., et al. 2009, A&A, 507, 1257

Giovannini, G., Feretti, L., & Andernach, H. 1985, A&A, 150, 302

Giovannini, G., Feretti, L., & Stanghellini, C. 1991, A&A, 252, 528

Giovannini, G., Tordi, M., & Feretti, L. 1999, New Astronomy, 4, 141

Giovannini, G., Cau, M., Bonafede, A., et al. 2020, A&A, 640, A108

Gladders, M. D., López-Cruz, O., Yee, H. K. C., & Kodama, T. 1998, ApJ, 501, 571

Gladders, M. D., & Yee, H. K. C. 2000, ApJ, 120, 2148

Golovich, N., Dawson, W. A., Wittman, D. M., et al. 2019, ApJ, 882, 69

González, J. D. R., Sharon, K., Reed, B., et al. 2020, ApJ, 902, 44

Hamaker, J., Bregman, J., & Sault, R. 1996, A&A, 117, 137

Hoang, D. N., Brüggen, M., Botteon, A., et al. 2022, A&A, 665, A60

Hoekstra, H., Bartelmann, M., Dahle, H., et al. 2013, Space Sci. Rev., 177, 75

Högbom, J. A. 1974, A&AS, 14, 417

Jaffe, W. J. 1977, ApJ, 212, 1

Jansen, F., Lumb, D., Altieri, B., et al. 2001, A&A, 365, L1

Jansky, K. 1932, Proc. IRE, 20, 1920

—. 1935, Proc. IRE, 23, 1158

Jonas, J. L., & MeerKAT Team. 2016, in MeerKAT Science: On the Pathway to the SKA, ed. R. Taylor, F. Camilo, L. Leeuw, & K. Moodley (Trieste: PoS), 1

Józsa, G. I. G., White S. V., Thorat K., et al. 2020, ASPC, 527, 635

Kahniashvili, T., Maravin, Y., Natarajan, A., Battaglia, N., & Tevzadze, A. G. 2013, ApJ, 770, 47

Kale, R., Venturi, T., Giacintucci, S., et al. 2013, A&A, 557, A99

—. 2015, A&A, 579, A92

Kang, H., Jones, T. W., & Gieseler, U. D. J. 2002, ApJ, 579, 337

Kang, H., & Ryu, D. 2011, ApJ, 734, 18

Kapferer, W., Ferrari C., Domainko W., et al. 2006, A&A, 447, 827

Kenyon, J. S., Smirnov, O. M., Grobler, T. L., & Perkins, S. J. 2018, MNRAS, 478, 2399

Kim, J., Jee, M. J., Perlmutter, S., et al. 2019, ApJ, 887, 76

Knowles, K., Baker, A. J., Bond, J. R., et al. 2019, MNRAS, 486, 1332

Kraus, J. D. 1986, Radio Astronomy (Powell: Cygnus-Quasar Books)

Kravtsov, A. V., & Borgani, S. 2012, ARA&A, 50, 353

Large, M. I., Mathewson, D. S., & Haslam, C. G. T. 1959, Nature, 183, 1663

Limousin, M., Morandi, A., Sereno, M., et al. 2013, Space Sci. Rev., 177, 155

Lin, Y.-T., Mohr, J. J., & Stanford, S. A. 2003, ApJ, 591, 749

Lindner, R. R., Baker, A. J., Hughes, J. P., et al. 2014, ApJ, 786, 49

Lynds, R., & Petrosian, V. 1986, BAAS, 18, 1014

López-Cruz, O., Barkhouse, W. A., & Yee, H. K. C. 2004, ApJ, 614, 679

Martinez Aviles, G., Johnston-Hollitt, M., Ferrari, C., et al. 2018, A&A, 611, A94

Mauch, T., Cotton, W. D., Condon, J. J., et al. 2020, ApJ, 888, 61

McMullin, J. P., Waters B., Schiebel D., Young W., & Golap K. 2007, ASPC, 376, 127

Menanteau, F., Hughes, J. P., Sifón, C., et al. 2012, ApJ, 748, 7

Meneghetti, M., Rasia, E., Merten, J., et al. 2010, A&A, 514, A93

Mhlahlo, N., & Jamrozy, M. 2021, MNRAS, 508, 2910

Mo, H., van den Bosch, F., & White, S. 2010, Galaxy Formation and Evolution (New York: Cambridge University Press)

Molnar, S. 2016, FrASS, 2, 7M

Murgia, M., Govoni, F., Markevitch, M., et al. 2009, A&A, 499, 679

Ness, J.-U., Parmar, A., Valencic, L., et al. 2014, ASNA, 335, 210

Noordam, J. E. 2004, in Ground-based Telescopes, ed. J. M. O. Jr., Vol. 5489, International Society for Optics and Photonics, 817 – 825

Nunhokee, C. D., Bernardi, G., Manti, S., et al. 2017, Radio multifrequency observations of galaxy clusters. The Abell 399–401 pair, arXiv:2102.02900

Offringa, A. R., McKinley, B., Hurley-Walker, N., et al. 2014, MNRAS, 444, 606

Offringa, A. R., & Smirnov, O. 2017, MNRAS, 471, 301

Orrù, E., Murgia, M., Feretti, L., et al. 2007, A&A, 467, 943

Parekh, V., van der Heyden, K., Ferrari, C., Angus, G., & Holwerda, B. 2015, A&A, 575, A127

Pearce, C. J. J., van Weeren, R. J., Andrade-Santos, F., et al. 2017, ApJ, 845, 81

Peebles, P. J. E. 1980, The large-scale structure of the universe (Princeton: Princeton University Press)

Perley, R. A., & Butler, B. J. 2017, ApJS, 230, 7

Petrosian, V. 2001, ApJ, 557, 560

Pierre, M., Pacaud, F., Adami, C., et al. 2016, A&A, 592, A1

Pinzke, A., Pfrommer, C., & Bergström, L. 2011, Phys. Rev. D, 84, 123509

Planck Collaboration, Ade, P. A. R., Aghanim, N., et al. 2014, A&A, 571, A20

—. 2015, A&A, 581, A14

—. 2016, A&A, 594, A27

Planck Collaboration, Aghanim, N., Akrami, Y., et al. 2020, A&A, 641, A6

Planelles, S., Schleicher, D. R. G., & Bykov, A. M. 2016, Large-Scale Structure Formation: From the First Non-linear Objects to Massive Galaxy Clusters, ed. A. Balogh, A. Bykov, J. Eastwood, & J. Kaastra (New York, NY: Springer New York), 93–139

Pratt, G. W., Croston, J. H., Arnaud, M., & Böhringer, H. 2009, A&A, 498, 361

Rajpurohit, K., Brunetti, G., Bonafede, A., et al. 2021, A&A, 646, A135

Rasia, E., Meneghetti, M., Martino, R., et al. 2012, New Journal of Physics, 14, 055018

Rau, U., & Cornwell, T. J. 2011, A&A, 532, A71

Reber, G. 1940, ApJ, 91, 62

—. 1942, Proc. IRE, 30, 367

Rees, M. J. 1987, QJRAS, 28, 197

—. 2006, ASNA, 327, 395

Reynolds, J. 1994, ATNF Technical Memos, AT/39.3/040

Ricker, P. M., & Sarazin, C. L. 2001, ApJ, 561, 621

Rykoff, E. S., Rozo, E., Busha, M. T., et al. 2014, ApJ, 785, 104

Ryle, M., & Vonberg, D. 1946, Nature, 158, 339

Sarazin, C. L. 1988, X-ray emission from clusters of galaxies (Cambridge: Cambridge University Press)

Schellenberger, G., Giacintucci, S., Lovisari, L., et al. 2022, ApJ, 925, 91

Schwab, F. R. 1984, AJ, 89, 1076

Smirnov, O. M. 2011, A&A, 527, A106

Smirnov, O. M., & Tasse, C. 2015, MNRAS, 449, 2668

Springel, V. 2005, MNRAS, 364, 1105

Springel, V., White, S. D. M., Jenkins, A., et al. 2005, Nature, 435, 629

Sunyaev, R. A., & Zel'dovich, Y. B. 1972, CoASP, 4, 173

Tasse, C., Hugo, B., Mirmont, M., et al. 2018, A&A, 611, A87

Thompson, A. R. 1999, ASPC, 180, 11

Thompson, A. R., Moran, J. M., & Swenson, G. W. J. 2017, Interferometry and Synthesis in Radio Astronomy, 3rd edn. (Cham: Springer)

van Weeren, R. J., Brüggen, M., Röttgering, H. J. A., & Hoeft, M. 2011, MNRAS, 418, 230

van Weeren, R. J., de Gasperin, F., Akamatsu, H., et al. 2019, Space Sci. Rev., 215, 16

van Weeren, R. J., Röttgering, H. J. A., Brüggen, M., & Cohen, A. 2009, A&A, 505, 991

Vazza, F., Brunetti, G., & Gheller, C. 2009, Mem. S.A.It. Suppl., 13, 151

Venturi, T., Giacintucci, S., Brunetti, G., et al. 2007, A&A, 463, 937

Venturi, T., Giacintucci, S., Cassano, R., et al. 2009, ASPC, 407, 232

Xu, J., & Han, J. L. 2022, ApJ, 926, 65

Yeap, K. H., Loh, M. C., Tham, C. Y., et al. 2016, AEM, 3, 32

Zhang, C., Churazov, E., Forman, W. R., & Lyskova, N. 2019, MNRAS, 488, 5259

Zohren, H., Schrabback, T., van der Burg, R. F. J., et al. 2019, MNRAS, 488, 2523

Zwicky, F. 1933, Helvetica Physica Acta, 6, 110